

Colossal angular magnetoresistance in ferrimagnetic nodal-line semiconductors

<https://doi.org/10.1038/s41586-021-04028-7>

Received: 7 April 2021

Accepted: 15 September 2021

Published online: 24 November 2021

 Check for updates

Junho Seo^{1,2,14}, Chandan De^{1,3,14}, Hyunsoo Ha^{4,14}, Ji Eun Lee^{5,14}, Sungyu Park¹, Joonbum Park⁶, Yurii Skourski⁶, Eun Sang Choi⁷, Bongjae Kim⁸, Gil Young Cho^{1,2,9}, Han Woong Yeom^{1,2}, Sang-Wook Cheong^{3,10}, Jae Hoon Kim⁵✉, Bohm-Jung Yang^{4,11,12}✉, Kyo Kim¹³✉ & Jun Sung Kim^{1,2}✉

Efficient magnetic control of electronic conduction is at the heart of spintronic functionality for memory and logic applications^{1,2}. Magnets with topological band crossings serve as a good material platform for such control, because their topological band degeneracy can be readily tuned by spin configurations, dramatically modulating electronic conduction^{3–10}. Here we propose that the topological nodal-line degeneracy of spin-polarized bands in magnetic semiconductors induces an extremely large angular response of magnetotransport. Taking a layered ferrimagnet, $\text{Mn}_3\text{Si}_2\text{Te}_6$, and its derived compounds as a model system, we show that the topological band degeneracy, driven by chiral molecular orbital states, is lifted depending on spin orientation, which leads to a metal–insulator transition in the same ferrimagnetic phase. The resulting variation of angular magnetoresistance with rotating magnetization exceeds a trillion per cent per radian, which we call colossal angular magnetoresistance. Our findings demonstrate that magnetic nodal-line semiconductors are a promising platform for realizing extremely sensitive spin- and orbital-dependent functionalities.

The recent development of topological materials and their fascinating transport phenomena have opened a new avenue for utilizing topologically protected quantum states in electronic and spintronic applications with low dissipation and high reliability^{3–10}. In particular, topological magnets^{3–26}, where both magnetism and nontrivial band topology coexist, have emerged as promising candidates to realize such novel functionalities, because their topological band degeneracy and the relevant charge or spin transport are highly sensitive to spin configurations and can be drastically modulated by external perturbations. Prominent examples include the giant anomalous Hall effect due to the significantly enhanced Berry curvature in ferromagnetic nodal-line semimetals^{11–18} and the quantum anomalous Hall effect in bulk-insulating topological ferromagnets with quantized dissipationless conduction^{21–26}. The key challenge lies in finding new topological magnets whose topological bands entirely dictate charge or spin conduction and are efficiently controllable by magnetization, which may lead to unprecedented magnetotransport functionalities with extreme sensitivity.

We propose that magnetic nodal-line semiconductors are such an example. In ferromagnetic nodal-line semimetals, including Fe_3GeTe_2 , $\text{Co}_3\text{Sn}_2\text{S}_2$ and Co_2MnGa (refs. ^{11–18}), the band crossing points of the spin-polarized bands near the Fermi level (E_F) are protected by crystal-line symmetry and form a line in the momentum space. When the

spin–orbit coupling (SOC) is taken into account, opening and closing of the SOC gap (Δ_{SOC}) is determined by the relative orientation between orbital angular momentum (\mathbf{L}), fixed along a certain crystal axis, and spin direction (\mathbf{S}), rotatable by external magnetic fields (Fig. 1a). In particular, the nodal line with Δ_{SOC} acts as a one-dimensional source of Berry curvature, resulting in the giant anomalous Hall effect^{11–18}. A related but distinct behaviour is expected in ferromagnetic semiconductors if the spin-polarized conduction or valence bands possess a topological nodal-line degeneracy. In such ferromagnetic nodal-line semiconductors, the SOC lifts the band degeneracy and pushes one of the bands towards E_F by $\Delta_{\text{SOC}}/2$, depending on the relative orientations of \mathbf{L} and \mathbf{S} (Fig. 1b). Therefore, when the bandgap Δ and Δ_{SOC} are comparable, spin rotation by external magnetic fields drastically modulates the bandgap and thus charge conduction, leading to large angular magnetoresistance (MR). Here we present such a case in a layered ferrimagnetic semiconductor, $\text{Mn}_3\text{Si}_2\text{Te}_6$, revealing an unprecedentedly large angular MR of $\sim 10^9$ times difference with rotating magnetization, which we call colossal angular MR.

Topological nodal-line band degeneracy

$\text{Mn}_3\text{Si}_2\text{Te}_6$ is in a self-intercalated van der Waals structure with trigonal symmetry, where the hexagonal MnSiTe_3 layers and the triangular Mn

¹Center for Artificial Low Dimensional Electronic Systems, Institute for Basic Science (IBS), Pohang, Korea. ²Department of Physics, Pohang University of Science and Technology (POSTECH), Pohang, Korea. ³Laboratory of Pohang Emergent Materials, Pohang Accelerator Laboratory, Pohang, Korea. ⁴Department of Physics and Astronomy, Seoul National University, Seoul, Korea. ⁵Department of Physics, Yonsei University, Seoul, Korea. ⁶Hochfeld-Magnetlabor Dresden (HLD-EMFL), Helmholtz-Zentrum Dresden-Rossendorf, Dresden, Germany. ⁷National High Magnetic Field Laboratory, Florida State University, Tallahassee, FL, USA. ⁸Department of Physics, Kunsan National University, Gunsan, Korea. ⁹Asia Pacific Center for Theoretical Physics, Pohang, Korea. ¹⁰Rutgers Center for Emergent Materials and Department of Physics & Astronomy, Rutgers University, Piscataway, NJ, USA. ¹¹Center for Correlated Electron Systems, Institute for Basic Science (IBS), Seoul, Korea. ¹²Center for Theoretical Physics (CTP), Seoul National University, Seoul, Korea. ¹³Korea Atomic Energy Research Institute (KAERI), Daejeon, Korea. ¹⁴These authors contributed equally: Junho Seo, Chandan De, Hyunsoo Ha, Ji Eun Lee. ✉e-mail: super@yonsei.ac.kr; bjang@snu.ac.kr; kyoo@kaeri.re.kr; js.kim@postech.ac.kr

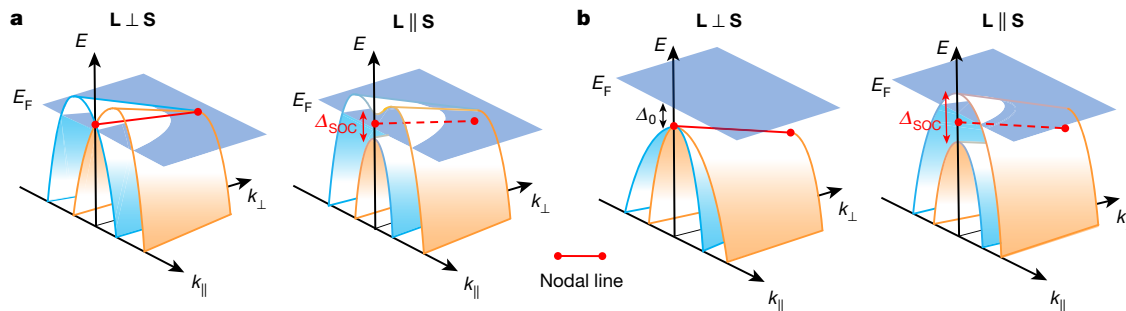


Fig. 1 | Magnetic nodal-line semimetal and semiconductor. **a, b**, The nodal-line structure along the symmetry line for magnetic nodal-line semimetals (**a**) and nodal-line semiconductors (**b**). The orbital degrees of freedom of spin-polarized bands are indicated by different colours (orange and blue). The orbital-driven band degeneracy occurs along the nodal line (red solid line), which can be lifted by the SOC with $\Delta_{\text{SOC}} \propto \mathbf{L} \cdot \mathbf{S}$. In magnetic nodal-line semimetals (**a**), opening the SOC gap for $\mathbf{L} \parallel \mathbf{S}$ makes the nodal line

(dashed line) act as a one-dimensional source of Berry flux in the momentum space, resulting in a large anomalous Hall effect. In magnetic nodal-line semiconductors (**b**), the electronic gap Δ remains intact for $\mathbf{L} \perp \mathbf{S}$ in the presence of the SOC, while the lifting of nodal-line band degeneracy for $\mathbf{L} \parallel \mathbf{S}$ pushes one of the bands towards the Fermi level. This induces the insulator-to-metal transition, controlled by the relative orientation of \mathbf{S} against \mathbf{L} , resulting in colossal angular MR.

layers are alternately stacked (Fig. 2a, b)^{27–29}. The localized spins ($S = 5/2$) of Mn atoms in the hexagonal (Mn1) and triangular (Mn2) layers have strong antiferromagnetic (AFM) interlayer interaction, which dominates over the intralayer AFM interaction between Mn1 spins. Thus, Mn1 spins within the plane prefer to be aligned ferromagnetically and are coupled antiferromagnetically with Mn2 spins²⁹, forming a ferrimagnetic order (Fig. 2a) below a critical temperature (T_c) of 78 K. The corresponding electronic structure of ferrimagnetic $\text{Mn}_3\text{Si}_2\text{Te}_6$, calculated using density functional theory, has an electronic gap between the spin-polarized Te p valence and Mn d conduction bands (Fig. 2c and Supplementary Fig. 1a). This bandgap is found to be sensitive to the total magnetization of Mn spins due to different Mn d -Te p hybridization^{30,31} and can be closed in a hypothetical ferromagnetic phase with parallel Mn1 and Mn2 spins (Supplementary Fig. 1b, c). Thus, a ferrimagnetic-to-ferromagnetic transition at high magnetic fields, in principle, can induce an insulator-to-metal transition. However, we found no signature of such a magnetic transition, at least, up to $H = 70$ T owing to the strong interlayer AFM interaction (Extended Data Fig. 6).

Alternatively, the nodal-line structure of the valence Te band and its strong SOC can lead to the insulator-to-metal transition within the ferrimagnetic phase, as we proposed in Fig. 1b. First, we identified that without SOC, the C_{3v} trigonal point group symmetry of $\text{Mn}_3\text{Si}_2\text{Te}_6$ permits 2 two-dimensional irreducible representations along the ΓA line, and the Te p orbital bands with E_g character form a twofold degenerate nodal line along the k_z axis. To understand this topological nodal line carrying quantized π Berry phase, it is sufficient to consider a single Te triangular layer, trimerized owing to the Mn atoms, with a unit cell containing three Te atoms (Fig. 2d and Supplementary Note 2). We decompose the in-plane p orbitals of the j th Te atom into the radial $|p_{r,j}\rangle$ and tangential $|p_{t,j}\rangle$ components, where $j \in \{1, 2, 3\}$ indicates the three sublattice sites (Fig. 2e). Considering C_{3z} symmetry along the k_z axis, we choose a degenerate basis for the E_g states (that is, the right-handed (R) and left-handed (L) orthogonal basis states), $|p_r, R\rangle = (1/\sqrt{3}) \sum_{j=1}^3 w^j |p_{r,j}\rangle$ and $|p_t, L\rangle = (1/\sqrt{3}) \sum_{j=1}^3 w^{-j} |p_{t,j}\rangle$ ($i = r, t$) with C_{3z} eigenvalues of w and w^2 ($w = e^{i\frac{2\pi}{3}}$), respectively. These R and L states are time-reversal conjugate as $\mathbf{T}|p_r, R\rangle = |p_t, L\rangle$ (\mathbf{T} , time-reversal operator), and carry orbital angular momentum $+1$ and -1 , respectively. As the p_r and p_t orbitals can be mixed, these states for the E_g valence band at the Γ point can generally be written as $|\mathbf{R}\rangle = \alpha|p_r, R\rangle + \beta|p_t, L\rangle$ and $|\mathbf{L}\rangle = \mathbf{T}|\mathbf{R}\rangle$, where α and β are material-specific parameters (Supplementary Note 3). This introduces four degenerate states $|\mathbf{R}, \uparrow\rangle$, $|\mathbf{L}, \uparrow\rangle$, $|\mathbf{R}, \downarrow\rangle$ and $|\mathbf{L}, \downarrow\rangle$, described by spin polarization in the $+z$ ($-z$) direction \uparrow (\downarrow) and the chirality (R, L) degrees of freedom. Then, owing to the ferrimagnetic ordering with magnetization m along the \hat{n} direction, these states are split into two pairs of spin-polarized states with the corresponding Hamiltonian

$\mathbf{H}_{\text{FM}} = m(\hat{s} \cdot \hat{n}) \otimes \tau_0$, where s_i and τ_j are the Pauli matrices for the spin and chirality degrees of freedom. Therefore, the orbital-driven chirality (R, L) degrees of freedom result in twofold nodal-line degeneracy of the spin-polarized Te valence bands (Fig. 2f and Supplementary Notes 4 and 5).

Having established the nodal-line degeneracy in the valence bands of $\text{Mn}_3\text{Si}_2\text{Te}_6$, now we consider the effect of atomic SOC. The SOC term $\mathbf{S} \cdot \mathbf{L}$ yields the Hamiltonian $\mathbf{H}_{\text{SOC}} = \gamma s_z \otimes \tau_z$ where $\gamma = i(\alpha\beta^* - \alpha^*\beta)$. Only the $S_z L_z$ term ($L_z |c\rangle$) can contribute to this Hamiltonian, because $\langle p_a | L_b | p_c \rangle = i\epsilon_{abc}$, where $a, b, c \in \{x, y, z\}$, $\hbar = 1$, and only the in-plane p orbitals are relevant to the Te E_g band. The in-plane magnetization ($M \parallel ab$) with $\hat{n} = \cos\theta\hat{x} + \sin\theta\hat{y}$ gives $\Delta\mathbf{H} = \mathbf{H}_{\text{FM}} + \mathbf{H}_{\text{SOC}} = m(\cos\theta s_x + \sin\theta s_y) \otimes \tau_0 + \gamma s_z \otimes \tau_z$. As $\Delta\mathbf{H}$ commutes with $s_0 \otimes \tau_z$, the states $|\psi\rangle$ and $s_0 \otimes \tau_z |\psi\rangle$ are always degenerate, preserving the twofold degeneracy of the spin-polarized E_g states (Fig. 2g). However, for $M \parallel c$ with $\hat{n} = \hat{z}$, the spin-dependent part of the Hamiltonian becomes $\Delta\mathbf{H} = \mathbf{H}_{\text{FM}} + \mathbf{H}_{\text{SOC}} = m s_z \otimes \tau_0 + \gamma s_z \otimes \tau_z$ which lifts the twofold degeneracy of the spin-polarized bands. Thus, the lifting of nodal-line band degeneracy is controlled by spin orientation. Consistently, band calculations show that the canting of $\langle \mathbf{s} \rangle$ towards the c axis increases the SOC-induced band splitting up to ~ 300 meV along the nodal line and eventually closes the bandgap (Fig. 2h). These observations imply that spin orientation works as a magnetic valve, switching between the metallic and insulating states in the same ferrimagnetic phase.

Metal–insulator transition by spin rotation

To experimentally demonstrate a metal–insulator transition with spin rotation, we investigated the transport properties of $\text{Mn}_3\text{Si}_2\text{Te}_6$, both undoped and doped with 6% Ge at the Si sites or 20% Se at the Te sites. As confirmed by the magnetic susceptibility $\chi(T)$ and the field-dependent magnetization $M(H)$ at $T = 2$ K, $T_c = 78$ K and the net magnetic moment $M_{\text{sat}} \sim 1.5 \mu_B$, lying on the ab plane, are nearly the same for the undoped and doped samples (Extended Data Fig. 2). Consistent with our calculations (Fig. 2g), a semiconducting behaviour is observed for $M_{\text{sat}} \parallel ab$ in the resistivity $\rho_{ab}(T)$ curves at low temperatures, well described by the Arrhenius equation $\rho_{ab}(T) = \rho_0 \exp(\Delta/k_B T)$. The resulting activation gap Δ for the undoped, Ge-doped and Se-doped samples is -4 , -12 and -25 meV, respectively, smaller than the calculated gap of -120 meV. This indicates that the activation gap is determined by impurity (acceptor) bands close to the valence bands (Fig. 3a), as typically found in lightly doped semiconductors³², which is consistent with the crossover from the activation-type to the variable-range hopping (VRH)-type conduction at low temperatures (Extended Data Fig. 3)^{33–35}.

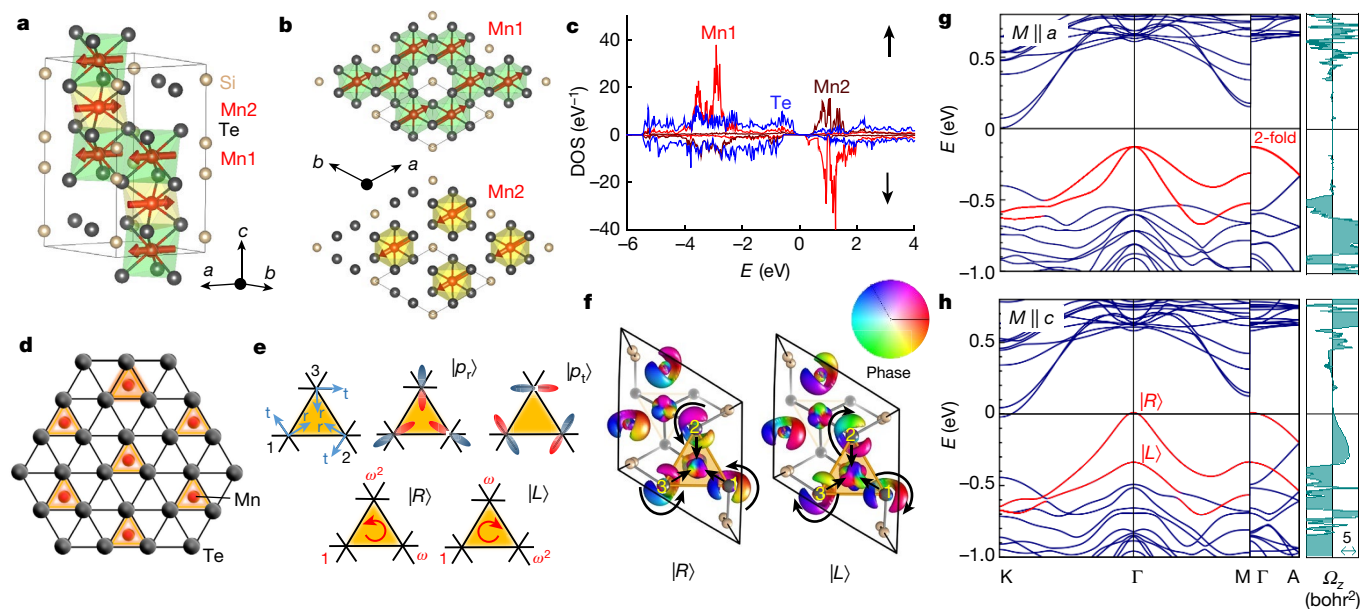


Fig. 2 | Nodal-line band degeneracy of the chiral orbital states in $\text{Mn}_3\text{Si}_2\text{Te}_6$. **a, b**, Crystal and magnetic structure of $\text{Mn}_3\text{Si}_2\text{Te}_6$. The Mn atoms are at the centre of the MnTe_6 octahedra (coloured regions), which form honeycomb (Mn1) and triangular (Mn2) layers, stacked along the c axis (**a**). Within each Mn layer, spins are ferromagnetically aligned in the plane, while spins of adjacent Mn1 and Mn2 layers are antiferromagnetically coupled (**b**). **c**, Calculated spin-dependent DOS for the majority (\uparrow) and minority (\downarrow) spins. The Te states, hybridized with the Mn states, have a much wider bandwidth than the Mn1 and Mn2 states, split by exchange interaction. **d**, Structure of a single Te layer. Grey

and red circles denote Te atoms and Mn dimers, respectively. **e**, Description of the chiral molecular orbitals $|R\rangle$ and $|L\rangle$ with orbital angular momentum $+1$ and -1 , which are linear combinations of local $|p_i\rangle$ orbitals of three Te atoms in a trimerized unit cell. **f**, Calculated wavefunctions of the SOC-split bands at the Γ point for $M \parallel c$. For the chiral molecular states, $|R, \uparrow\rangle$ and $|L, \uparrow\rangle$, the phase winding directions at each Te atom are anticlockwise and clockwise, respectively, as presented by the colour code and arrows. **g, h**, Calculated band structures and Berry curvature Ω_z with SOC for $M \parallel a$ (**g**) and $M \parallel c$ (**h**).

By applying out-of-plane magnetic fields ($H \parallel c$) up to the saturation field $H_{\text{sat}} \sim 10$ T, we can continuously rotate M_{sat} towards the c axis, while keeping the ferrimagnetic order intact (Extended Data Fig. 2). For $H \parallel c$, $\rho_{ab}(T)$ of the undoped $\text{Mn}_3\text{Si}_2\text{Te}_6$ systematically and drastically decreases with H and eventually shows the metallic behaviour above the critical field $H_c \sim 4$ T, much smaller than H_{sat} (Fig. 3e). Similar trends are observed in Ge-doped $\text{Mn}_3\text{Si}_2\text{Te}_6$ (Fig. 3f) with $H_c \sim 8$ T, while Se-doped $\text{Mn}_3\text{Si}_2\text{Te}_6$ shows an incomplete suppression of the upturn of $\rho_{ab}(T)$, presumably due to smaller SOC strength (Fig. 3g). In contrast, for $H \parallel ab$, the semiconducting behaviour is maintained, even under high fields up to ~ 30 T (Extended Data Fig. 6) without any difference of $\rho_{ab}(T)$ between the cases of $H \perp I$ and $H \parallel I$ (Extended Data Fig. 7a). Moreover, for given H and θ , we estimate the tilting angle of magnetization (θ_M), depicted in the inset of Fig. 3e, taking into account the in-plane magnetic anisotropy (Extended Data Table 1). For undoped $\text{Mn}_3\text{Si}_2\text{Te}_6$, we found that $\rho_{ab}(H \parallel c)$ and $\rho_{ab}(H, \theta)$ curves collapse into a single curve as a function of θ_M (Fig. 3b), suggesting that the main control parameter is neither the magnetic field strength nor its orientation against the current direction, but the tilting angle θ_M of the magnetization towards the c axis (Fig. 3b).

The contrasting field-induced variation of the activation gap $\Delta(H)$ for $H \parallel c$ and $H \parallel ab$ can be estimated by the exponential increase in $\rho_{ab}(T)$ at different magnetic fields, using the Arrhenius equation (Extended Data Fig. 5). For $H \parallel ab$ up to $H = 14$ T, $\Delta(H)$ only slightly decreases by ~ 1.5 meV for both undoped and doped samples (Fig. 3c). This is due to suppression of spin fluctuation by external in-plane fields, as manifested by a slight increase of magnetization (Extended Data Fig. 2). However, on increasing $H \parallel c$, $\Delta(H)$ rapidly decreases to zero at $H_c \sim 4$ T and 8 T for the undoped and Ge-doped samples, respectively. The Se-doped sample exhibits a similar reduction of $\Delta(H)$ yet with a small residual gap. As the tilting angle θ_M increases with $H \parallel c$, $\Delta(H)$ is expected to be reduced with $H \parallel c$ below the critical field H_c , in good agreement with experiment (Fig. 3c). Moreover, we found that

in total, 22 $\rho_{ab}(T)$ curves showing the semiconducting behaviour ($d\rho_{ab}/dT < 0$), taken from all of the samples at different fields, collapse onto a single curve in the normalized plot with ρ_{ab}/ρ_0 and $k_B T/\Delta$ (Fig. 3d). Thus, rather than extrinsic scattering, it is the activation gap, sensitive to the magnetization orientation, that actually dictates charge conduction in $\text{Mn}_3\text{Si}_2\text{Te}_6$.

Our spectroscopic evidence further confirms the contrasting gap modulation with different magnetic field orientations. For undoped $\text{Mn}_3\text{Si}_2\text{Te}_6$, the absorption spectra as a function of incident photon energy were obtained at $T = 1.5$ K by using terahertz time-domain spectroscopy. At $H = 0$, the absorption coefficient is significantly suppressed at low energies, consistent with gap opening in $\text{Mn}_3\text{Si}_2\text{Te}_6$. Under small magnetic fields up to 1.8 T for $H \parallel c$, the absorption spectra rapidly shift to lower energies, filling up the optical gap (Fig. 3h), manifesting the insulator-to-metal transition, consistent with the transport results (Fig. 3e). This contrasts with the case of $H \parallel ab$ showing a minor shift of absorption spectra even with $H \sim 7$ T (Fig. 3i). The same trend with magnetic field is observed for Ge- or Se-doped samples (Extended Data Fig. 8). These spectroscopic results unambiguously prove our proposal on the genuine electronic-structure origin of the metal-insulator transition induced by rotating magnetization in $\text{Mn}_3\text{Si}_2\text{Te}_6$.

Colossal angular MR

The most striking consequence of controlled lifting of band degeneracy in magnetic nodal-line semiconductors is a huge change in the resistivity under rotating magnetic fields. Figure 4a shows the angle-dependent $\rho_{ab}(\theta)$ with $I \parallel a$ and the rotating H from $H \parallel ab$ ($\theta = 0^\circ$) to $H \parallel c$ ($\theta = 90^\circ$) (Fig. 3e). Dramatic variation of $\rho_{ab}(\theta)$ by $\sim 10^4$ times difference is observed at $H = 5$ T for the undoped $\text{Mn}_3\text{Si}_2\text{Te}_6$, yielding the colossal angular MR, quantified by $(1/\rho_{\text{min}}) d\rho(\theta)/d\theta$, up to $\sim 10^{11}\%$ per radian (Fig. 4a). With increasing temperature up to T_c , the angular

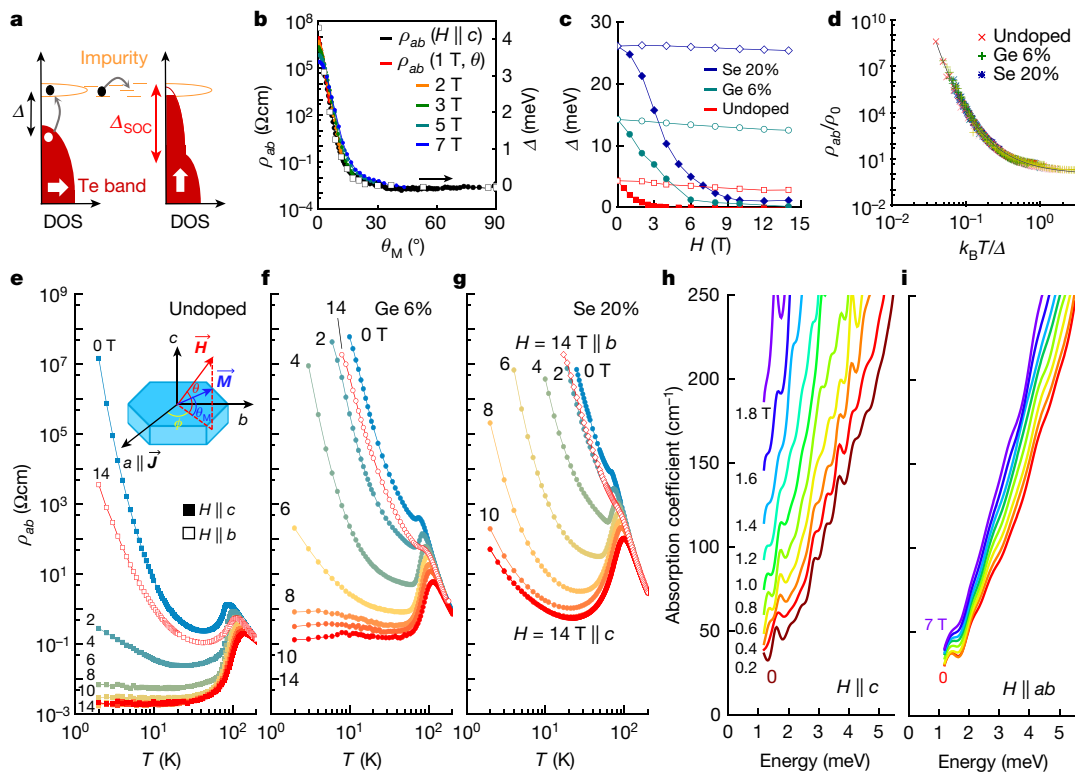


Fig. 3 | Metal–insulator transition by spin orientation. **a**, Electronic structure of $\text{Mn}_3\text{Si}_2\text{Te}_6$ with impurity states. With spin rotation from the in-plane to the out-of-plane directions, the electronic gap Δ is closed owing to lifting of band degeneracy by the SOC gap Δ_{SOC} . **b**, In-plane resistivity $\rho_{ab}(H||c)$ and $\rho_{ab}(H, \theta)$ (filled symbols) of the undoped sample as a function of the tilting angle of magnetization θ_M at $T = 2$ K. For comparison, the activation field $\Delta(\theta_M)$ (open symbols) is also plotted. The tilting angles of the magnetic field (θ) and magnetization (θ_M) with respect to the ab plane are shown in the inset of **e**. **c**, Magnetic-field-dependent activation gap $\Delta(H)$ for $H||c$ (filled symbols) and $H||ab$ (open symbols) for the undoped, Ge- and Se-doped samples. The errors in the experimental data are smaller than the size of the points. **d**, Scaling plot of

the normalized resistivity ρ_{ab}/ρ_0 and temperature $k_B T/\Delta$ for all of the samples with different magnetic fields. In total, 22 curves are collapsed onto a single curve (black line). **e–g**, Temperature-dependent resistivity $\rho_{ab}(T)$ of undoped (**e**), Ge-doped (**f**) and Se-doped (**g**) $\text{Mn}_3\text{Si}_2\text{Te}_6$ under magnetic fields up to 14 T with different orientations. For $H||c$ (filled symbols), $\rho_{ab}(T)$ is rapidly suppressed and becomes metallic at high fields, whereas it remains semiconducting for $H = 14$ T $|| ab$ (red open symbols). **h, i**, Absorption coefficient as a function of photon energy for undoped $\text{Mn}_3\text{Si}_2\text{Te}_6$ taken at $T = 1.5$ K for $H||c$ (**h**) and $H||ab$ (**i**). The absorption spectra shift rapidly to lower energies and fill up the gap with $H = 1.8$ T $|| c$, while the spectra weakly depend on $H||ab$ up to 7 T.

MR is gradually suppressed but remains much larger than the typical anisotropic MR found in other magnets^{36,37}. For Ge- or Se-doped samples, a similar behaviour of $\rho_{ab}(H, \theta)$ is observed at $H = 14$ T, and the resulting colossal angular MR is expected to be even larger, beyond our measurement limit. Using the scaling behaviour of $\rho_{ab}(T)$ (Fig. 3d), we estimate the maximum resistivity at $H = 6$ T and $T = 6.5$ K for the Ge-doped sample and at $H = 10$ T and $T = 12$ K for the Se-doped sample, confirming the angular MR larger than $-10^{11}\%$ per radian, which is the largest angular MR ever reported, to our knowledge, among magnetic materials, as summarized in Fig. 4b.

Finally, we compare the angular MRs of various magnets and discuss their mechanisms. Figure 4b presents the maximum value of the angular MR $(1/\rho_{\min})d\rho(\theta)/d\theta$ and the MR $\Delta\rho/\rho(H)$ at a given magnetic field, where ρ_{\min} is the minimum angle-dependent resistivity. Although the angular MR is typically a few per cent in most ferromagnetic metals^{36,38}, a large angular MR is observed up to 200% per radian in transition metal oxides, such as orthorhombic perovskite manganites^{39,40} or Sr_2IrO_4 (ref. 37), and up to $-10^{5\%}$ per radian in the recently discovered AFM semiconductors EuCd_2P_2 (ref. 41), EuMnSb_2 (ref. 42) and EuTe_2 (refs. 43,44). In a topological magnet candidate, CeAlGe (ref. 19), the large angular MR up to $-10^{3\%}$ per radian is also observed due to the highly resistive domain wall formation. For all of the aforementioned cases, the underlying mechanisms for the angular MR are associated with magnetic-field-induced phase transitions, and thus the working windows for H or T are limited to the relatively narrow regions near

the phase transition (Extended Data Table 2 and Extended Data Fig. 7k). However, in magnetic nodal-line semiconductors, the lifting of the topological band degeneracy and the resulting angular MR are controlled by spin rotation without involving magnetic phase transitions, consistent with the nearly linear dependence of the angular MR and $\Delta\rho/\rho(H)$. Thus, the working H range can be reduced well below the saturation field H_{sat} , and the T range can be extended nearly up to T_c , as demonstrated by $\text{Mn}_3\text{Si}_2\text{Te}_6$ (Fig. 4b and Extended Data Fig. 7).

Our findings highlight that in magnetic nodal-line semiconductors, spin orientation tunes the orbital-driven topological band degeneracy and thus works as an effective magnetic valve for current flow. The key parameters determining the angular sensitivity are the SOC gap size, magnetocrystalline anisotropy and the energy position of the nodal-line degeneracy, which can be further optimized by chemical doping, as partly demonstrated in Fig. 4a, or other external perturbations such as strain or pressure. We envision various spintronic applications of magnetic nodal-line semiconductors, such as extremely sensitive vector magnetic sensing or efficient electrical readout of spin information. Furthermore, exploiting the semiconducting nature, the electric field gating enables effective and low-power control of the colossal angular MR, together with possible modulation of T_c or magnetic anisotropy. These unique characters establish magnetic nodal-line semiconductors to be a promising platform to realize extremely sensitive spin- or orbital-dependent functionalities.

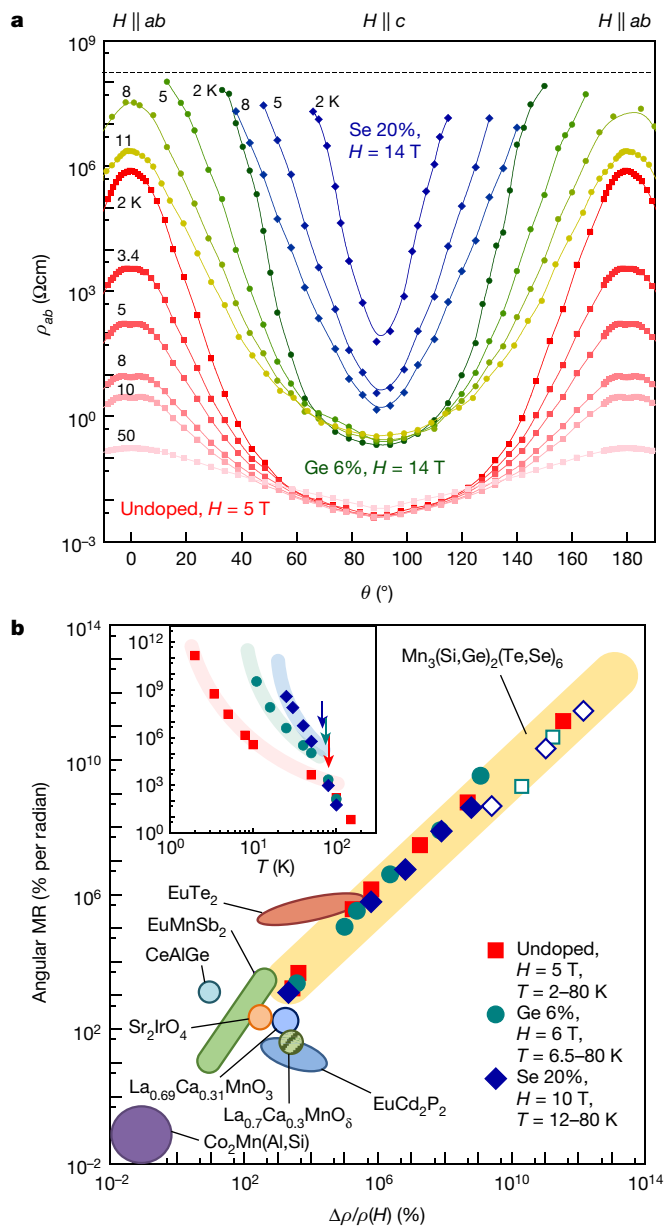


Fig. 4 | Colossal angular MR. **a**, Angular response of $\rho_{ab}(\theta)$ for the undoped, Ge-doped and Se-doped $\text{Mn}_3\text{Si}_2\text{Te}_6$ crystals as a function of the magnetic field orientation θ at different temperatures. For the doped samples, the resistivity taken at $H = 14$ T and low temperatures is beyond the measurement limit (dashed line) near $H \parallel ab$. **b**, Maximum angular MR $\frac{d}{d\theta} \left(\frac{\rho(\theta)}{\rho_{\min}} \right)$ and MR $\Delta\rho/\rho(H)$ of the undoped, Ge-doped and Se-doped $\text{Mn}_3\text{Si}_2\text{Te}_6$ crystals under $T \leq T_c$ and different magnetic fields. Colossal angular MR exceeding a trillion per cent per radian is measured (filled symbols) or estimated (open symbols) by the resistivity scaling shown in Fig. 3d. For comparison, we also plot the data for representative magnetic materials, showing a large MR and angular MR^{19,37–44}. Inset: temperature-dependent angular MR for both undoped and doped $\text{Mn}_3\text{Si}_2\text{Te}_6$. The ferrimagnetic transition temperatures are indicated by the arrows.

Note added in proof: After submission of this manuscript, one paper has been published reporting similar magnetotransport properties of undoped $\text{Mn}_3\text{Si}_2\text{Te}_6$ (ref. 45).

Online content

Any methods, additional references, Nature Research reporting summaries, source data, extended data, supplementary information,

acknowledgements, peer review information; details of author contributions and competing interests; and statements of data and code availability are available at <https://doi.org/10.1038/s41586-021-04028-7>.

- Žutić, I., Fabian, J. & Das Sarma, S. Spintronics: fundamentals and applications. *Rev. Mod. Phys.* **76**, 323–410 (2004).
- Fert, A. Nobel lecture: Origin, development, and future of spintronics. *Rev. Mod. Phys.* **80**, 1517–1530 (2008).
- Hasan, M. Z. & Kane, C. L. Colloquium: Topological insulators. *Rev. Mod. Phys.* **82**, 3045–3067 (2010).
- Qi, X.-L. & Zhang, S.-C. Topological insulators and superconductors. *Rev. Mod. Phys.* **83**, 1057–1110 (2011).
- Wang, J. & Zhang, S. C. Topological states of condensed matter. *Nat. Mater.* **16**, 1062–1067 (2017).
- Armitage, N. P., Mele, E. J. & Vishwanath, A. Weyl and Dirac semimetals in three-dimensional solids. *Rev. Mod. Phys.* **90**, 015001 (2018).
- Manna, K., Sun, Y., Muechler, L., Kübler, J. & Felser, C. Heusler, Weyl and Berry. *Nat. Rev. Mater.* **3**, 244–256 (2018).
- Nagaosa, N., Morimoto, T. & Tokura, Y. Transport, magnetic and optical properties of Weyl materials. *Nat. Rev. Mater.* **5**, 621–636 (2020).
- Kumar, N., Guin, S. N., Manna, K., Shekhar, C. & Felser, C. Topological quantum materials from the viewpoint of chemistry. *Chem. Rev.* **121**, 2780–2815 (2021).
- Narang, P., Garcia, C. A. & Felser, C. The topology of electronic band structures. *Nat. Mater.* **20**, 293–300 (2021).
- Liu, E. et al. Giant anomalous Hall effect in a ferromagnetic kagome-lattice semimetal. *Nat. Phys.* **14**, 1125–1131 (2018).
- Okamura, Y. et al. Giant magneto-optical responses in magnetic Weyl semimetal $\text{Co}_2\text{Sn}_2\text{S}_6$. *Nat. Commun.* **11**, 4619 (2020).
- Ding, L. et al. Intrinsic anomalous Nernst effect amplified by disorder in a half-metallic semimetal. *Phys. Rev. X* **9**, 041061 (2019).
- Sakai, A. et al. Giant anomalous Nernst effect and quantum-critical scaling in a ferromagnetic semimetal. *Nat. Phys.* **14**, 1119–1124 (2018).
- Xu, L. et al. Anomalous transverse response of Co_2MnGa and universality of the room-temperature $\alpha_{ij}^A/\sigma_{ij}^A$ ratio across topological magnets. *Phys. Rev. B* **101**, 180404 (2020).
- Li, P. et al. Giant room temperature anomalous Hall effect and tunable topology in a ferromagnetic topological semimetal Co_2MnAl . *Nat. Commun.* **11**, 3476 (2020).
- Ye, L. et al. Massive Dirac fermions in a ferromagnetic kagome metal. *Nature* **555**, 638–642 (2018).
- Kim, K. et al. Large anomalous Hall current induced by topological nodal lines in a ferromagnetic van der Waals semimetal. *Nat. Mater.* **17**, 794–799 (2018).
- Suzuki, T. et al. Singular angular magnetoresistance in a magnetic nodal semimetal. *Science* **365**, 377–381 (2019).
- Sakai, A. et al. Iron-based binary ferromagnets for transverse thermoelectric conversion. *Nature* **581**, 53–57 (2020).
- Chang, C. Z. et al. Experimental observation of the quantum anomalous Hall effect in a magnetic topological insulator. *Science* **340**, 167–170 (2013).
- Checkelsky, J. G. et al. Trajectory of the anomalous Hall effect towards the quantized state in a ferromagnetic topological insulator. *Nat. Phys.* **10**, 731–736 (2014).
- Yasuda, K. et al. Quantized chiral edge conduction on domain walls of a magnetic topological insulator. *Science* **358**, 1311–1314 (2017).
- Yasuda, K. et al. Large non-reciprocal charge transport mediated by quantum anomalous Hall edge states. *Nat. Nanotechnol.* **15**, 831–835 (2020).
- Chang, C. Z. et al. High-precision realization of robust quantum anomalous Hall state in a hard ferromagnetic topological insulator. *Nat. Mater.* **14**, 473–477 (2015).
- Deng, Y. et al. Quantum anomalous Hall effect in intrinsic magnetic topological insulator MnBi_2Te_4 . *Science* **367**, 895–900 (2020).
- Rimet, R., Schlenker, C. & Vincent, H. A new semiconducting ferrimagnet: a silicon manganese telluride. *J. Magn. Magn. Mater.* **25**, 7–10 (1981).
- Vincent, H., Leroux, D., Bijaoui, D., Rimet, R. & Schlenker, C. Crystal structure of $\text{Mn}_3\text{Si}_2\text{Te}_6$. *J. Solid State Chem.* **63**, 349–352 (1986).
- May, A. F. et al. Magnetic order and interactions in ferrimagnetic $\text{Mn}_3\text{Si}_2\text{Te}_6$. *Phys. Rev. B* **95**, 174440 (2017).
- Kanamori, J. & Terakura, K. A general mechanism underlying ferromagnetism in transition metal compounds. *J. Phys. Soc. Jpn* **70**, 1433–1434 (2001).
- Jungwirth, T., Sinova, J., Mašek, J., Kučera, J. & MacDonald, A. H. Theory of ferromagnetic (III,Mn)V semiconductors. *Rev. Mod. Phys.* **78**, 809–864 (2006).
- Yu, P. Y. & Cardona, M. *Fundamentals of Semiconductors* (Springer, 2005).
- Sharma, S. K., Sagar, P., Gupta, H., Kumar, R. & Mehra, R. M. Meyer-Neldel rule in Se and S-doped hydrogenated amorphous silicon. *Solid State Electron.* **51**, 1124–1128 (2007).
- Durá, O. J. et al. Transport, electronic, and structural properties of nanocrystalline CuAlO_2 delafossites. *Phys. Rev. B* **83**, 045202 (2011).
- Hauser, A. J. et al. Electronic and magnetic tunability of $\text{Sr}_2\text{CrReO}_6$ films by growth-mediated oxygen modulation. *Appl. Phys. Lett.* **102**, 032403 (2013).
- Kokado, S., Tsunoda, M., Harigaya, K. & Sakuma, A. Anisotropic magnetoresistance effects in Fe, Co, Ni, Fe_2N , and half-metallic ferromagnet: a systematic analysis. *J. Phys. Soc. Jpn* **81**, 024705 (2012).

37. Wang, H. et al. Giant anisotropic magnetoresistance and nonvolatile memory in canted antiferromagnet Sr_2IrO_4 . *Nat. Commun.* **10**, 2280 (2019).
38. Endo, T., Kubota, H. & Miyazaki, T. Magnetoresistance of $\text{Co}_2\text{MnAl}_{1-x}\text{Si}_x$ Heusler alloys. *J. Magn. Soc. Jpn* **23**, 1129–1132 (1999).
39. Eckstein, J. N., Bozovic, I., O'Donnell, J., Onellion, M. & Rzechowski, M. S. Anisotropic magnetoresistance in tetragonal $\text{La}_{1-x}\text{Ca}_x\text{MnO}_3$ thin films. *Appl. Phys. Lett.* **69**, 1312 (1996).
40. Li, R.-W. et al. Anomalously large anisotropic magnetoresistance in a perovskite manganite. *Proc. Natl Acad. Sci. USA* **106**, 14224–14229 (2009).
41. Wang, Z.-C. et al. Colossal magnetoresistance without mixed valence in a layered phosphide crystal. *Adv. Mater.* **33**, 2005755 (2021).
42. Soh, J.-R. et al. Magnetic and electronic structure of Dirac semimetal candidate EuMnSb_2 . *Phys. Rev. B* **100**, 174406 (2019).
43. Yin, J. et al. Large negative magnetoresistance in the antiferromagnetic rare-earth dichalcogenide EuTe_2 . *Phys. Rev. Mater.* **4**, 013405 (2020).
44. Yang, H. et al. Observation of an unusual colossal anisotropic magnetoresistance effect in an antiferromagnetic semiconductor. Preprint at <https://arxiv.org/abs/2103.02818> (2021).
45. Ni, Y. et al. Colossal magnetoresistance via avoiding fully polarized magnetization in the ferrimagnetic insulator $\text{Mn}_3\text{Si}_2\text{Te}_6$. *Phys. Rev. B* **103**, L161105 (2021).

Publisher's note Springer Nature remains neutral with regard to jurisdictional claims in published maps and institutional affiliations.

© The Author(s), under exclusive licence to Springer Nature Limited 2021

Single-crystal growth

Single crystals of pristine and 6%-Ge-doped $\text{Mn}_3\text{Si}_2\text{Te}_6$ were grown by the standard high-temperature self-flux technique. A mixture of Mn (99.95%), Si (99.999%) and Te (99.999%) in a molar ratio of 1:2:6 was placed in an alumina crucible, and another empty alumina crucible was kept on top of it with quartz wool separation. The whole crucible assembly was sealed in an evacuated quartz ampoule after a few purges with Ar. The ampoule was first heated in a muffle furnace up to 1,000 °C in 12 h and kept dwelling for 24 h to obtain a homogeneous solution. Subsequently, the furnace was slowly cooled down to 700 °C in 150 h and remained for 12 h at 700 °C for the annealing of the crystals. The ampoule was then quickly taken out of the furnace and centrifuged to separate the crystals from the fluxes. The obtained crystals were in a plate shape with a typical dimension of $3 \times 3 \times 0.5 \text{ mm}^3$. The pure $\text{Mn}_3\text{Si}_2\text{Te}_6$ crystal phase was confirmed by the (0 0 L) Bragg peaks at room temperature (Extended Data Fig. 1a), and lattice parameters were determined from the powder X-ray diffraction of crushed crystals as $a = b = 7.0349(3) \text{ \AA}$ and $c = 14.2550(4) \text{ \AA}$, which is consistent with a previous report²⁹. Further, the energy-dispersive spectroscopy (EDS; Extended Data Fig. 1b–e), performed in a high-resolution field-emission scanning electron microscope (JSM 7800F PRIME with Dual EDS, Hitachi), confirms the stoichiometry of Mn, Si and Te as 2.96, 1.95 and 6.09, respectively.

For the Ge-doped crystals, a similar method was adopted using Si and Ge (99.999%) in a 10:1 atomic ratio. The obtained crystals were shiny black and plate shaped with a width of 3 to 5 mm and a thickness of nearly 1 mm. The same structure with $\text{Mn}_3\text{Si}_2\text{Te}_6$ was confirmed by X-ray diffraction on (0 0 L) planes on single crystals (Extended Data Fig. 1a) and powder X-ray diffraction of crushed crystals, which yield the lattice parameters, $a = b = 7.0353(2) \text{ \AA}$ and $c = 14.2670(2) \text{ \AA}$. While there is no considerable change in the in-plane lattice parameters, the subtle increase of the c -axis lattice parameter is due to the bigger size of Ge. The atomic composition of Mn, Si, Ge and Te, obtained from EDS, is 2.88:2.01:0.13:5.98, confirming 6% Ge doping.

For the 20%-Se-doped crystals, we employed a standard chemical vapour transport technique. A mixture of Mn, Si, Te and Se (99.99%) was placed in a 4-cm-long conical alumina crucible, which was sealed in a -22-cm-long quartz tube. I_2 was used as a transport agent. A temperature gradient of 750 °C to 700 °C was maintained for 400 h for the crystal growth followed by cooling to room temperature at $70 \text{ }^\circ\text{C h}^{-1}$. Plate-shaped 3- to 5-mm-wide and nearly 0.5-mm-thick crystals were obtained. X-ray diffraction confirmed a single phase with the lattice parameters $a = b = 6.9810(7) \text{ \AA}$ and $c = 13.7475(13) \text{ \AA}$. The decrease in both in-plane and out-of-plane lattice parameters is due to the lower size of Se. Further, EDS showed the atomic composition of Mn, Si, Te and Se as 3.03:1.99:4.67:1.29, respectively.

Magnetic and transport property measurements

The in-plane resistivity was measured in the standard four-probe configuration using a physical property measurement system (PPMS-14 T, Quantum Design) for up to $H = 14 \text{ T}$ and a resistive magnet up to 32 T at the National High Magnetic Field Laboratory at Tallahassee, FL, USA. Magnetization was measured under the magnetic field along the ab plane and c axis using a vibrating sample magnetometer option of the physical property measurement system (PPMS-14T, Quantum Design). High-field magnetotransport properties of $\text{Mn}_3\text{Si}_2\text{Te}_6$ were measured using a Bitter magnet of up to 31.6 T at the National High Magnetic Field Laboratory, Tallahassee. High-field torque magnetometry was measured up to 70 T at the Dresden High Magnetic Field Laboratory, Dresden (Extended Data Fig. 6).

Magnetic properties

Ferrimagnetic phase transition is observed in the magnetic susceptibility $\chi(T)$ of the undoped, Ge-doped and Se-doped $\text{Mn}_3\text{Si}_2\text{Te}_6$ crystals

(Extended Data Fig. 2a–c). The transition temperature T_c is slightly reduced with doping, as summarized in Extended Data Table 1. Under magnetic fields up to $H = 14 \text{ T}$, the field-dependent magnetization $M(H)$ at $T = 2 \text{ K}$ exhibits strong anisotropy with the net magnetic moment $M_{\text{sat}} \sim 1.5 \mu_B$. For $H \parallel ab$, $M(H)$ is rapidly saturated at a small coercive field $H_c = 200 \text{ Oe}$ and then increases slowly with H . For $H \parallel c$, on the other hand, $M(H)$ increases almost linearly up to $H_{\text{sat}} \sim 10 \text{ T}$ and becomes nearly saturated, following the $M(H)$ curve for $H \parallel ab$ above H_{sat} . These field- and temperature-dependent behaviours indicate the easy-plane ferrimagnetic order, as illustrated in Fig. 1a. Therefore, up to $H = 14 \text{ T}$, the ferrimagnetic order remains intact, owing to the strong exchange interaction between Mn1 and Mn2 spins (Supplementary Note 1)²⁹, but the net magnetization can be rotated from the easy plane (ab plane) to the hard axis (c axis) under $H \parallel c$. The saturated moment M_{sat} and magnetic fields H_{sat} for $H \parallel c$ are nearly the same for the Ge- or Se-doped crystals (Extended Data Fig. 2d–f), which yield the magnetocrystalline energy $K \sim 0.7 \text{ J cm}^{-3}$, estimated from the relation of $H_{\text{sat}} = 2K/M_{\text{sat}}$ (Extended Data Table 1). Above H_{sat} , $M(H)$ slowly increases without any signature of the spin-flop transition, which is further confirmed by high-field experiments, discussed below (Extended Data Fig. 6).

Electronic conduction in the absence of magnetic fields

In lightly doped semiconductors, electronic conduction is generally described by band- or hopping-type conduction. At relatively high temperatures, thermal activation of charge carriers between the localized impurity states and the delocalized conduction or valence bands dictates electronic conduction. This band conduction is described by the Arrhenius model as $\rho_{ab}(T) \propto \exp(\Delta/k_B T)$, where Δ is the gap between the localized and degenerate states. At low temperatures, however, thermal energy is not sufficient to induce charge excitations to the degenerate bands, and electron hopping takes place between remote impurity sites with the localized states near E_F , which leads to the VRH conduction. In the VRH models, the resistivity is described by the equation $\rho_{ab}(T) \propto \exp(T_0/T)^p$, where T_0 is a characteristic energy scale, determined by the localization length, and p is an exponent differentiating the types of VRH mechanisms. In the Mott-VRH model, assuming a constant density of states (DOS) near E_F , the exponent p is set by the dimensionality (D) of the system, as $p = 1/(D + 1)$. On the other hand, when Coulomb interaction between localized electrons suppresses the low-energy DOS, the exponent is $p = 1/2$ in all dimensions, which is called the Efros–Shklovskii (ES) VRH model. Usually in lightly doped semiconductors, the crossover occurs from the activation-type conduction to one of the VRH-type conduction with decreasing temperature.

Such a crossover behaviour is observed for all of the samples: undoped, 6%-Ge-doped and 20%-Se-doped $\text{Mn}_3\text{Si}_2\text{Te}_6$ crystals. Extended Data Fig. 3a–c shows the temperature-dependent $\rho_{ab}(T)$ as a function of $1/T$. Consistent with our electronic-structure calculations (Fig. 2g, h and Supplementary Note 1), all of the samples exhibit the semiconducting behaviour above and below T_c , except just below T_c , where a dip in $\rho_{ab}(T)$ is observed due to suppression of spin fluctuations, as typically found in itinerant magnets^{46,47}. At low temperatures, $\rho_{ab}(T)$ is well described by the activation model, $\rho_{ab}(T) \propto \exp(\Delta/k_B T)$ with activation gap $\Delta \approx 4.3, 14.2$ and 26.0 meV , for the undoped, 6%-Ge-doped and 20%-Se-doped samples, respectively. However, on further lowering the temperature (for example, below $T \leq 6 \text{ K}$ for the undoped sample), $\rho_{ab}(T)$ starts to deviate from the thermally activated semiconducting behaviour and shows the crossover to the VRH-type conduction. In Extended Data Fig. 3d–f, we plot $\rho_{ab}(T)$ as a function of $1/T^p$ with $p = 1/4, 1/3$ and $1/2$, which corresponds to the Mott-VRH models with three and two dimensions, and the ES-VRH model, respectively. The ES-VRH model shows better agreement with the measured $\rho_{ab}(T)$ than the Mott-VRH models, and the characteristic energy scale $T_0 \sim 1,444\text{--}8,591 \text{ K}$ is found to be comparable with those found in other lightly doped semiconductors, including thin films of Sr_2IrO_4 , Si and Ge (refs. 48–50). This crossover

behaviour, observed in both undoped and doped samples, indicates the presence of the impurity band, as illustrated in Fig. 3a.

In the paramagnetic phase above T_c , the semiconducting behaviour is maintained. For all of the samples, the gap energy is larger in the paramagnetic phase (Δ_{PM}) than in the ferrimagnetic phase (Δ ; Extended Data Table 1). As discussed in Supplementary Note 1, the bandgap of $Mn_3Si_2Te_6$ is mainly determined by two parameters; one is ferromagnetic correlation between the Mn spins, and the other is the SOC. The former shifts the band top of the valence bands with nodal-line degeneracy towards the Fermi level E_F with respect to the localized Mn states at high binding energy, while the latter lifts the nodal-line band degeneracy and pushes only one of the bands towards E_F by $\Delta_{SOC}/2$. In the paramagnetic phase, local exchange interaction remains finite, but the absence of long-range ferromagnetic order within the Mn1 layer significantly reduces the intralayer hopping strength and thus reduces the bandwidth of the valence state (Supplementary Note 1). This significantly enhances the bandgap of $Mn_3Si_2Te_6$, consistent with experiments.

Electronic conduction under magnetic fields

In itinerant ferromagnets or ferrimagnets, electronic conduction around T_c is mainly governed by spin fluctuations^{46,47}. Generally, external magnetic field suppresses thermally excited spin fluctuations near T_c and thus helps in stabilizing ferromagnetic or ferrimagnetic order with enhanced T_c . Extended Data Fig. 4a–f shows the temperature-dependent in-plane resistivity $\rho_{ab}(T)$ and its first derivative $d\rho_{ab}/dT$ at various magnetic fields for $H||ab$ and $H||c$. We determined T_c with the temperature at which $d\rho_{ab}(T)/dT$ exhibits a peak. The estimated T_c of undoped, Ge- and Se-doped $Mn_3Si_2Te_6$ monotonically increases with magnetic field for both field directions (Extended Data Fig. 4g–i). We found that T_c shifts to higher temperatures more rapidly for $H||c$ than $H||ab$ in the undoped and 6%-Ge-doped $Mn_3Si_2Te_6$. Considering the easy-plane magnetic anisotropy, the weaker enhancement of T_c for $H||ab$ than for $H||c$ is unusual, which requires further investigation.

At low temperatures, the semiconducting behaviour of $\rho_{ab}(T)$ shows strong dependence on magnetic field orientation. The field-dependent activation gap $\Delta(H)$ is extracted from the Arrhenius plots of $\rho_{ab}(T)$ for $H||ab$ and $H||c$ (Extended Data Fig. 5). For $H||ab$, the slope of $\rho_{ab}(T)$ in the Arrhenius plot changes slightly. This small change is related to suppression of spin fluctuation and thus a slight increase of the ferromagnetic correlation under external magnetic fields, consistent with magnetization curves under in-plane magnetic fields (Extended Data Fig. 2). In contrast, we observed dramatic reduction of the slope of $\rho_{ab}(T)$ for $H||c$ in all of the samples. The field-dependent activation gap $\Delta(H)$ consistently exhibits the distinct behaviours for $H||ab$ and $H||c$ in Extended Data Fig. 5d–f. These observations unambiguously confirm that the SOC-driven gap modulation with rotating magnetization is much more effective than the field-induced suppression of spin fluctuations.

Absence of magnetic-field-induced phase transition up to 70 T

Now we focus on the magnetic ground state at low temperatures under high magnetic fields. Under pulsed magnetic fields up to 70 T, we found no signature of the spin-flop transition in torque magnetometry $\tau(\theta, H)$ (Extended Data Fig. 6a). For different tilting angle θ of the external magnetic field against the c axis, $\tau(\theta, H)$ exhibits the monotonous field dependence without any noticeable anomaly. Consistently, the field-dependent magnetization $M(H)$ for $H||ab$ also monotonously increases with magnetic fields up to 60 T (Extended Data Fig. 6b). From the linear extrapolation of $M(H)$, the external magnetic field needed for full saturation of magnetic moments is estimated to be ~240 T. The absence of the spin-flop transition, at least, up to $H = 70$ T is consistent with the strong interlayer AFM interaction in $Mn_3Si_2Te_6$ (Supplementary Note 1)²⁹, which makes the ferrimagnetic order robust against external magnetic fields. Furthermore, in the MR measurements under static

magnetic fields up to 30 T for $H||ab$, we found that $Mn_3Si_2Te_6$ remains in the semiconducting regime (Extended Data Fig. 6c). This contrasts to the case of $H||c$, in which a magnetic field of only ~4 T is sufficient to induce the metallic state, confirming that the observed insulator-to-metal transition is not associated with a field-induced magnetic phase transition.

Angular MR

The angular MR of the undoped and doped $Mn_3Si_2Te_6$ strongly depends on temperature as shown in Extended Data Fig. 7. For the undoped $Mn_3Si_2Te_6$, angle-dependent $\rho_{ab}(T, \theta)$ under $H = 5$ T reveals that the maximum angular MR $(1/\rho_{min})d\rho(\theta)/d\theta$ decreases with increasing temperature, showing a clear kink at T_c , and rapidly diminishes above T_c (Extended Data Fig. 7). We found that up to T_c , the angular MR remains larger than ~10% per radian for both undoped and doped samples. As spin rotation under $H||c$ mainly determines the activation gap $\Delta(H)$ (Fig. 3b), the angular MR remains large at high magnetic fields above the critical field H_c , at which the activation gap is closed. As shown in Extended Data Fig. 7, the angular MR increases with H and then shows a saturation behaviour when $H > 3$ T for the undoped sample and $H > 6$ T (8 T) for the sample doped with 6% Ge (20% Se) (Extended Data Fig. 7k). Unlike other itinerant magnets whose angular MR is observed only in relatively narrow magnetic field and temperature ranges, $Mn_3Si_2Te_6$ exhibits the angular MR larger than 10% per radian in wide ranges of external parameters: magnetic fields larger than ~0.5 T, tilting angle of the magnetic field up to $|\theta| < 90^\circ$, temperature up to ~80 K (Extended Data Fig. 7). Furthermore, with chemical doping, the activation gap and the angular MR can be tuned (Extended Data Fig. 7j). This is because the band degeneracy is protected by the symmetry, and the SOC-driven gap modulation is relatively robust to external perturbations in magnetic nodal-line semiconductors (Extended Data Fig. 7 and Extended Data Table 2).

Terahertz absorption measurements

The terahertz absorption measurements were performed with a TERA K15 terahertz time-domain spectrometer (Menlo Systems) coupled with a SpectromagPT magneto-optical cryostat (Oxford Instruments). In the TERA K15, a femtosecond laser emits 90-fs pulses at a central wavelength of 1,560 nm with a 100 MHz repetition rate, and a terahertz pulse is generated from an InGaAs photoconductive emitter. After the terahertz pulse has passed through the sample, it is detected by an InGaAs photoconductive receiver. All terahertz optical paths were enclosed in a plexiglass box purged with nitrogen gas to eliminate water vapour absorption. The SpectromagPT system is a closed-cycle type and is operated in the temperature range of 1.5–300 K and the magnetic field range of 0–7 T. The $Mn_3Si_2Te_6$ crystals were fixed to a Au-coated Cu sample holder with Kapton tape. The time-dependent electric field waveform acquired by terahertz time-domain spectroscopy was converted to a complex-valued function (with both amplitude and phase) of frequency by using fast Fourier transformation.

Our terahertz time-domain spectroscopy measurements give spectroscopic evidence for the contrasting gap modulation with different magnetic field orientations in undoped or doped $Mn_3Si_2Te_6$. For the undoped sample at $H = 0$ T, we find that the temperature dependence of the absorption coefficient is not monotonic (Extended Data Fig. 8a, d, g): the absorption increases with temperature for 5–40 K (Extended Data Fig. 8a), decreases for 40–90 K (Extended Data Fig. 8d), but increases again for 90–300 K (Extended Data Fig. 8g). This temperature dependence is remarkably consistent with the resistivity $\rho_{ab}(T)$ exhibiting exactly the opposite pattern (Extended Data Fig. 4a). This implies that the non-monotonic temperature dependence of ρ_{ab} , especially the bump above 40 K, is intrinsic. For Ge- or Se-doped samples, we found that the change of absorption within 40–90 K is more suppressed, consistent with the observed weak bump in ρ_{ab} for Ge- or Se-doped samples (Extended Data Fig. 4b, c).

The in-plane (Extended Data Fig. 8j–l) and out-of-plane (Extended Data Fig. 8m–o) magnetic fields generate distinct behaviour of the terahertz absorption at $T = 1.5$ K. Under the in-plane field up to 7 T, there is a systematic, yet weak, redshift of the absorption onset, consistent with ρ_{ab} under in-plane field (Extended Data Fig. 4a–c). In stark contrast, under the out-of-plane field, the absorption increases while its onset redshifts rapidly, signalling the closing of the gap as expected from our transport data and theory. For undoped $\text{Mn}_3\text{Si}_2\text{Te}_6$, the gap essentially closes already at 1.8 T, well below the saturation field H_{sat} , indicating the touching of the valence band with the impurity level. The Ge- or Se-doped samples show the same trend with external magnetic fields but more insulating behaviour, consistent with the ρ_{ab} (Extended Data Fig. 4d–f). These observations unambiguously prove our proposal on the electronic-structure origin of the metal–insulator transition induced by magnetization rotation due to the nodal-line band degeneracy in $\text{Mn}_3\text{Si}_2\text{Te}_6$.

First-principles calculations

Electronic-structure calculations were performed with the full-potential local-orbital density functional theory calculation package⁵¹. The Perdew–Burke–Ernzerhof generalized gradient approximation functional was used for the exchange correlation functional, and relativistic effects were treated within a full four-component Dirac formalism. For the Brillouin zone integration, we used a $16 \times 16 \times 8$ k -point mesh in the full Brillouin zone. To obtain the maximally localized Wannier function and evaluate the Berry curvature, we used the pseudopotential plane-wave code Quantum Espresso⁵², combined with the Wannier90 and WannierBerri packages^{53,54}.

Data availability

The data that support the findings of this study are available from the corresponding authors on request.

46. Manyala, N. et al. Magnetoresistance from quantum interference effects in ferromagnets. *Nature* **404**, 581–584 (2000).
47. Tsujii, N., Nishide, A., Hayakawa, J. & Mori, T. Observation of enhanced thermopower due to spin fluctuation in weak itinerant ferromagnet. *Sci. Adv.* **5**, eaat5935 (2019).
48. Lu, C. et al. Crossover of conduction mechanism in Sr_2IrO_6 epitaxial thin films. *Appl. Phys. Lett.* **105**, 082407 (2014).
49. Yildiz, A., Serin, N., Serin, T. & Kasap, M. Crossover from nearest-neighbor hopping conduction to Efros–Shklovskii variable-range hopping conduction in hydrogenated amorphous silicon films. *Jpn. J. Appl. Phys.* **48**, 111203 (2009).

50. Li, Z. et al. Transition between Efros–Shklovskii and Mott variable-range hopping conduction in polycrystalline ermanium thin films. *Semicond. Sci. Technol.* **32**, 035010 (2017).
51. Koepernik, K. & Eschrig, H. Full-potential nonorthogonal local-orbital minimum-basis band-structure scheme. *Phys. Rev. B* **59**, 1743–1757 (1999).
52. Giannozzi, P. et al. QUANTUM ESPRESSO: a modular and open-source software project for quantum simulations of materials. *J. Phys. Condens. Matter* **21**, 395502 (2009).
53. Mostofi, A. A. et al. An updated version of wannier90: a tool for obtaining maximally-localised Wannier functions. *Comput. Phys. Commun.* **185**, 2309–2310 (2014).
54. Tsirkin, S. S. High performance Wannier interpolation of Berry curvature and related quantities with WannierBerri code. *npj Comput. Mater.* **7**, 33 (2021).

Acknowledgements We thank H. W. Lee and J. Y. Kim for productive discussion. We also thank H. G. Kim from the Pohang Accelerator Laboratory (PAL) for technical support. This work was supported by the Institute for Basic Science (IBS) through the Center for Artificial Low Dimensional Electronic Systems (no. IBS-R014-D1), and by the National Research Foundation of Korea (NRF) through the SRC (grant no. 2018R1A5A6075964), and the Max Planck-POSTECH Center for Complex Phase Materials (grant no. 2016K1A4A4A01922028). H.H. was supported by Samsung Science and Technology Foundation under project number SSTF-BA2002-06. The pulsed field work was supported by the HLD at HZDR, member of the European Magnetic Field Laboratory (EMFL). K.K. was supported by the NRF (grant no. 2016R1D1A1B02008461), and the internal R&D programme at KAERI (no. 524460-21). B.-J.Y. was supported by the Institute for Basic Science in Korea (grant no. IBS-R009-D1), Samsung Science and Technology Foundation under project number SSTF-BA2002-06, and NRF grants funded by the Korea government (MSIT; no. 2021R1A2C4002773 and no. NRF-2021R1A5A1032996). J.H.K. acknowledges financial support from the NRF through grant no. NRF-2021R1A2C3004989 and grant no. 2017R1A5A1014862 (vdWMRC SRC Program). B.K. acknowledges support by the NRF through grant no. 2021R1C1C1007017. S.-W.C. was partially supported by the Center for Quantum Materials Synthesis (cQMS), funded by the Gordon and Betty Moore Foundation’s EPIQS initiative through grant GBMF10104, and by Rutgers University. A portion of this work was performed at the National High Magnetic Field Laboratory, which is supported by the National Science Foundation Cooperative agreement no. DMR-1644779 and the State of Florida.

Author contributions J.S.K., J.S. and C.D. conceived the projects. J.S. and S.P. performed the transport measurements on bulk crystals. C.D., under the guidance of S.W.-C., synthesized the bulk crystals. H.H., B.K., K.K., G.Y.C. and B.-J.Y. performed the electronic-structure calculations and the band analysis. J.E.L. and J.H.K. conducted terahertz spectroscopy measurements and spectral analysis. J.P., Y.S. and E.S.C. conducted high-field experiments. G.Y.C. and H.W.Y. contributed to the data analysis. J.S., C.D., H.H., J.H.K., B.-J.Y., K.K. and J.S.K. co-wrote the manuscript. All authors discussed the results and commented on the paper.

Competing interests The authors declare no competing interests.

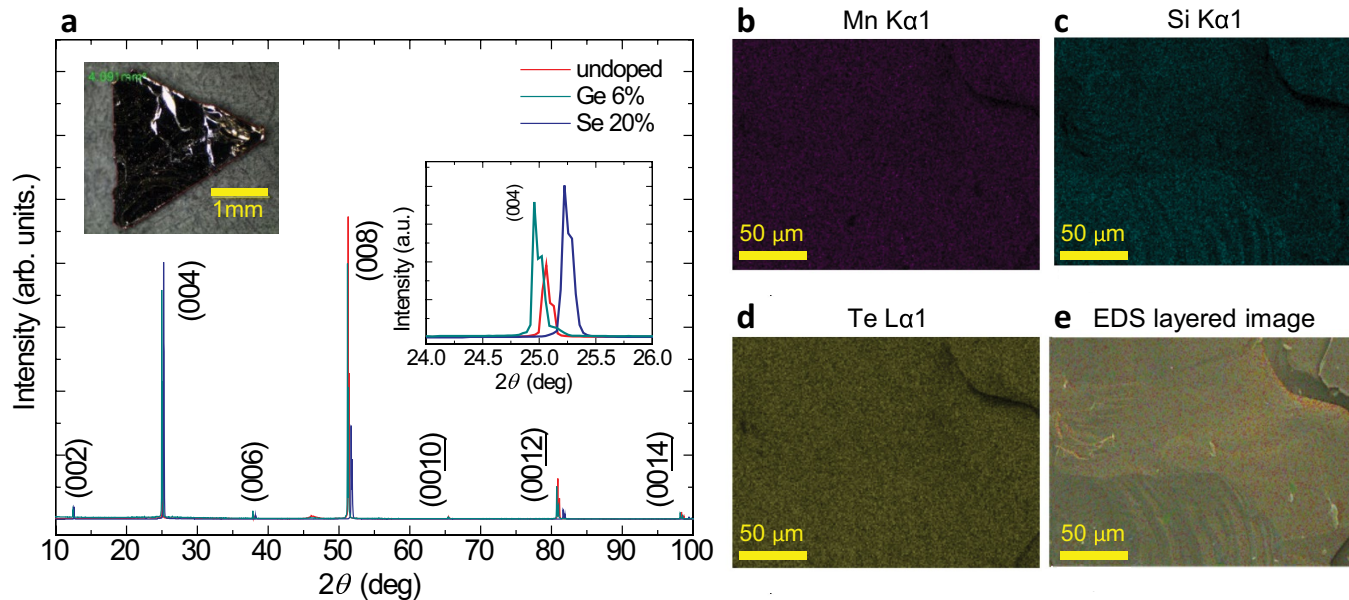
Additional information

Supplementary information The online version contains supplementary material available at <https://doi.org/10.1038/s41586-021-04028-7>.

Correspondence and requests for materials should be addressed to Jae Hoon Kim, Bohm-Jung Yang, Kyoo Kim or Jun Sung Kim.

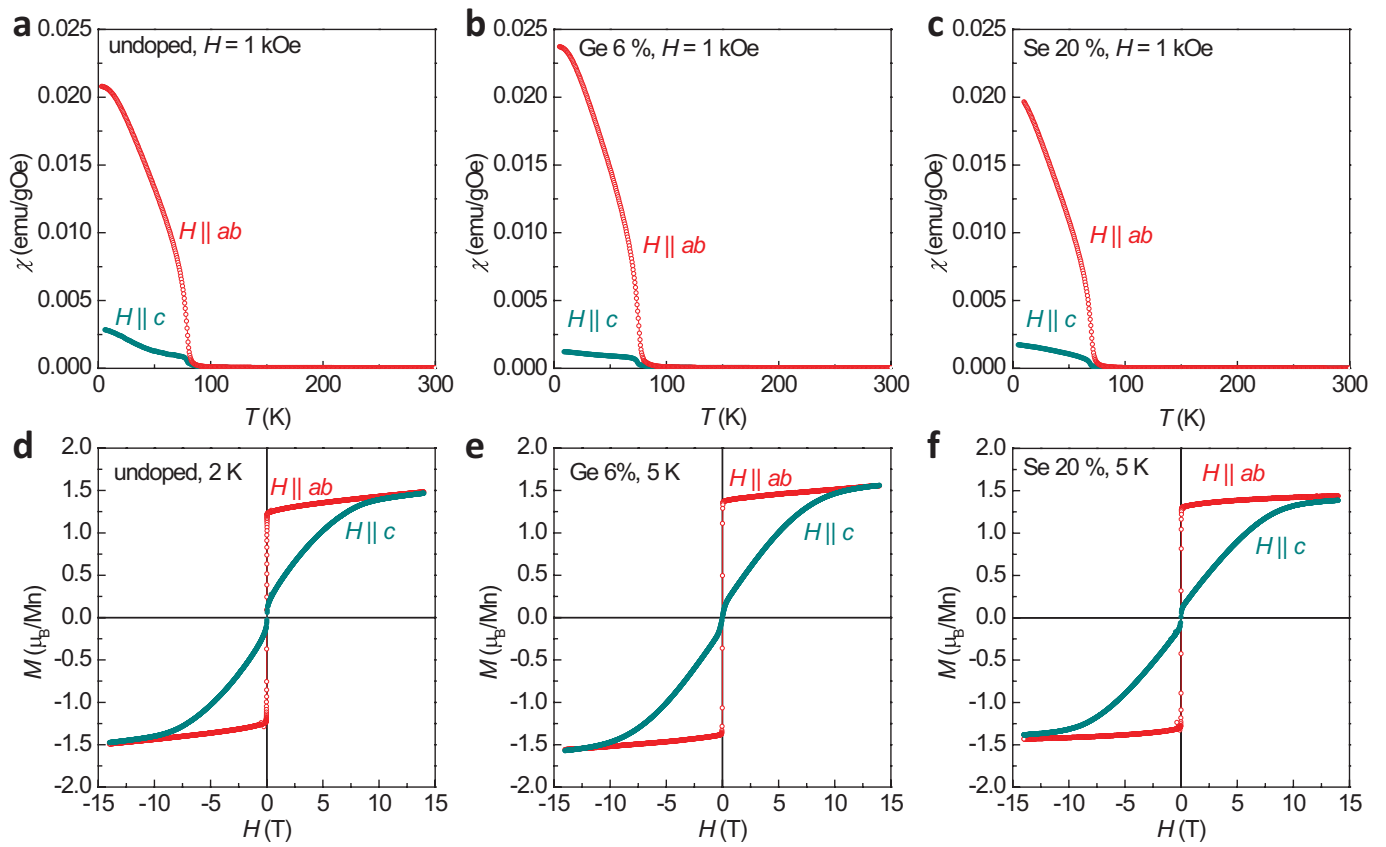
Peer review information Nature thanks Yong Xu and the other, anonymous, reviewer(s) for their contribution to the peer review of this work. Peer reviewer reports are available.

Reprints and permissions information is available at <http://www.nature.com/reprints>.



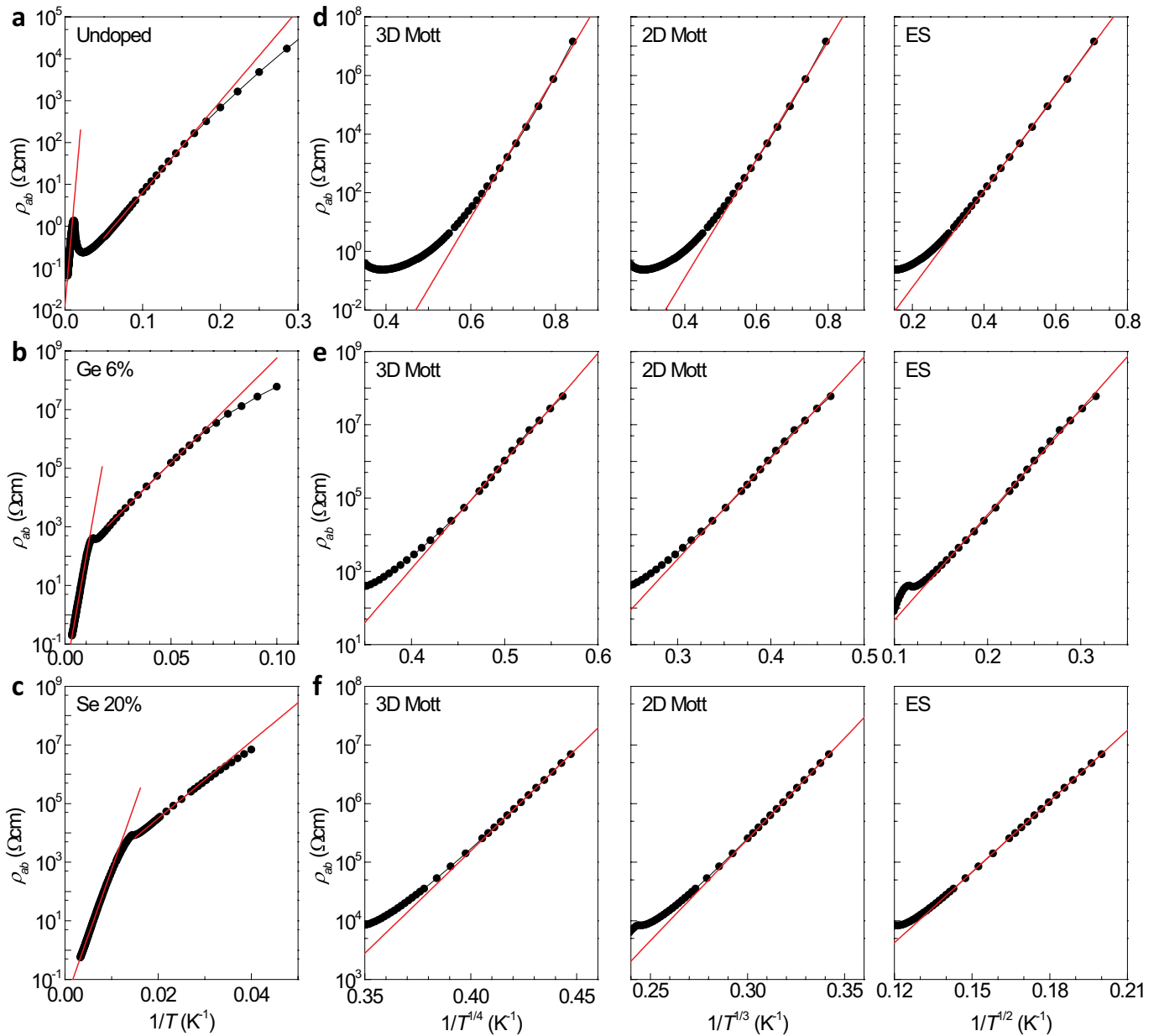
Extended Data Fig. 1 | Single crystal growth. **a**, X-ray diffraction pattern of the undoped, Ge- and Se-doped $\text{Mn}_3\text{Si}_2\text{Te}_6$ crystals recorded on (00L) plane at room temperature. The insets show a typical crystal image and a magnified X-ray diffraction data for Bragg peak (004). **b-d**, The energy dispersive

spectroscopy images on a selected area of $\text{Mn}_3\text{Si}_2\text{Te}_6$ crystal, taken at Mn $K\alpha 1$ (**b**), Si $K\alpha 1$ (**c**) and Te $L\alpha 1$ (**d**) edges. **e**, Combined Mn, Si and Te EDS image, showing a spatially uniform stoichiometry of $\text{Mn}_3\text{Si}_2\text{Te}_6$ crystal.



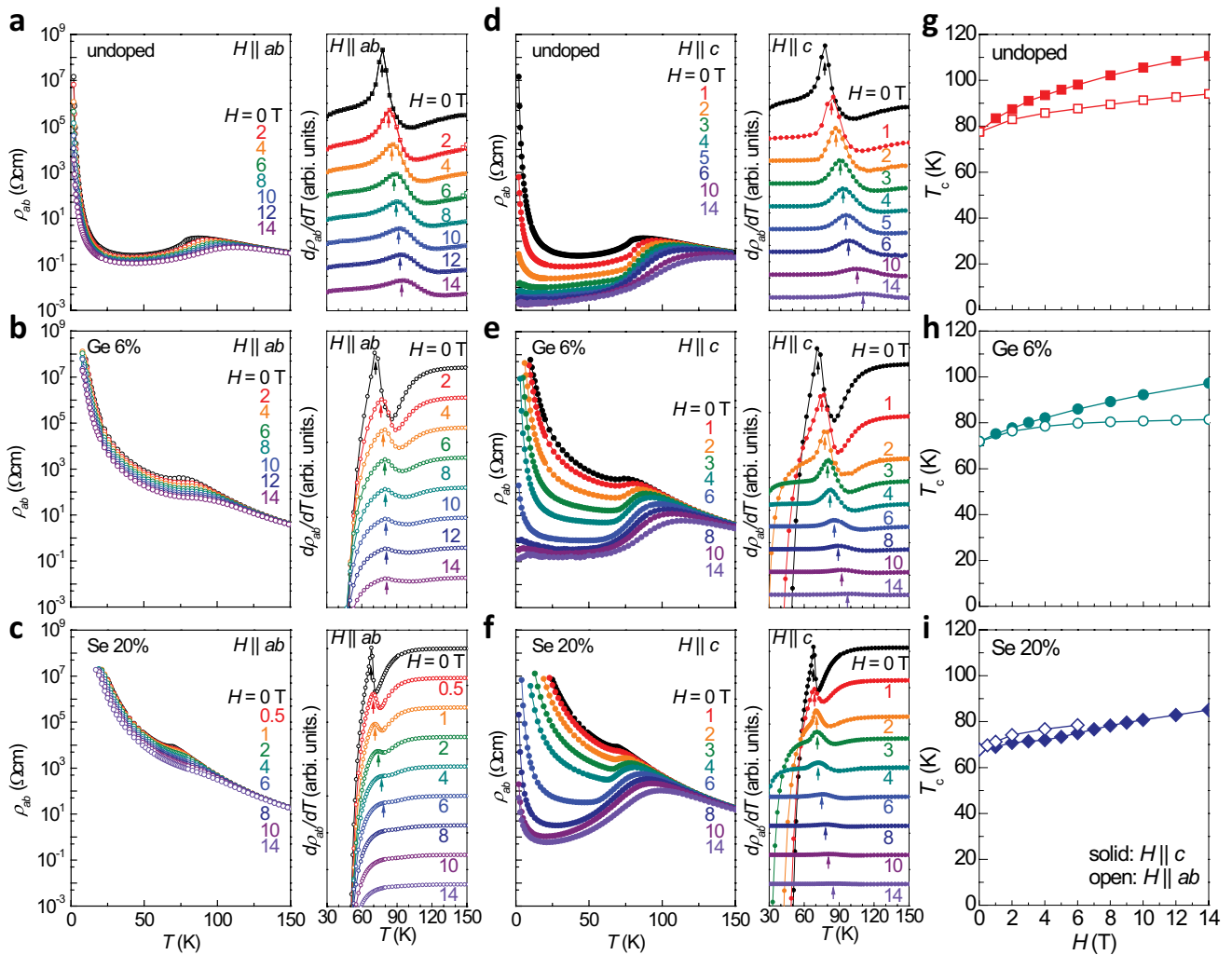
Extended Data Fig. 2 | Magnetic properties of $\text{Mn}_3\text{Si}_2\text{Te}_6$. a–c, Temperature dependent magnetic susceptibility $\chi(T)$ of undoped, Ge-doped and Se-doped $\text{Mn}_3\text{Si}_2\text{Te}_6$ single crystals for $H \parallel c$ (green) and $H \parallel ab$ (red) at $H = 1$ kOe. d–f,

Magnetic field-dependent magnetization $M(H)$ of undoped, Ge-doped and Se-doped $\text{Mn}_3\text{Si}_2\text{Te}_6$ single crystals for $H \parallel c$ (green) and $H \parallel ab$ (red) taken at $T = 2$ or 5 K.



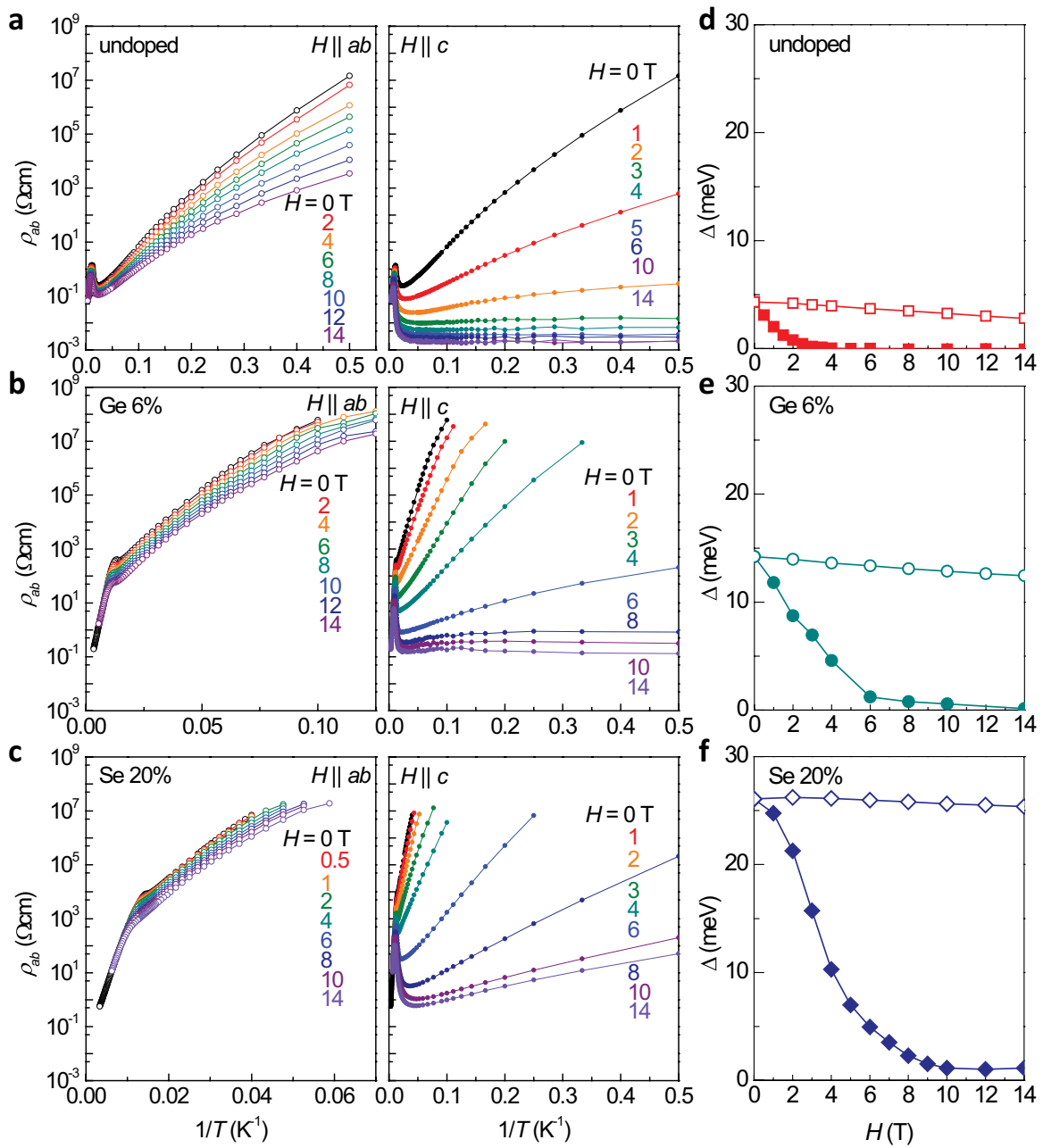
Extended Data Fig. 3 | Electronic conduction of $\text{Mn}_3\text{Si}_2\text{Te}_6$ at zero magnetic field. **a–c**, In-plane resistivity ρ_{ab} as a function of the inverse temperature for undoped (**a**), Ge-doped (**b**) and Se-doped (**c**) $\text{Mn}_3\text{Si}_2\text{Te}_6$ single crystals. Above and below T_c , $\rho_{ab}(T)$ follows the thermally activated semiconducting behaviour, described by $\rho_{ab}(T) \propto \exp(\Delta/k_B T)$ (red line), with different transport gap Δ (Extended Data Table 1). **d–f**, Variable-range hopping (VRH) conduction at low

temperatures for undoped (**d**), Ge-doped (**e**) and Se-doped (**f**) $\text{Mn}_3\text{Si}_2\text{Te}_6$ single crystals. The in-plane resistivity $\rho_{ab}(T)$ is plotted as a function of $1/T^p$ with exponents $p = 1/4$ (left), $1/3$ (middle), and $1/2$ (right), corresponding to the Mott-VRH models with three- and two-dimensions and the Efros-Shklovskii (ES) VRH model, respectively.



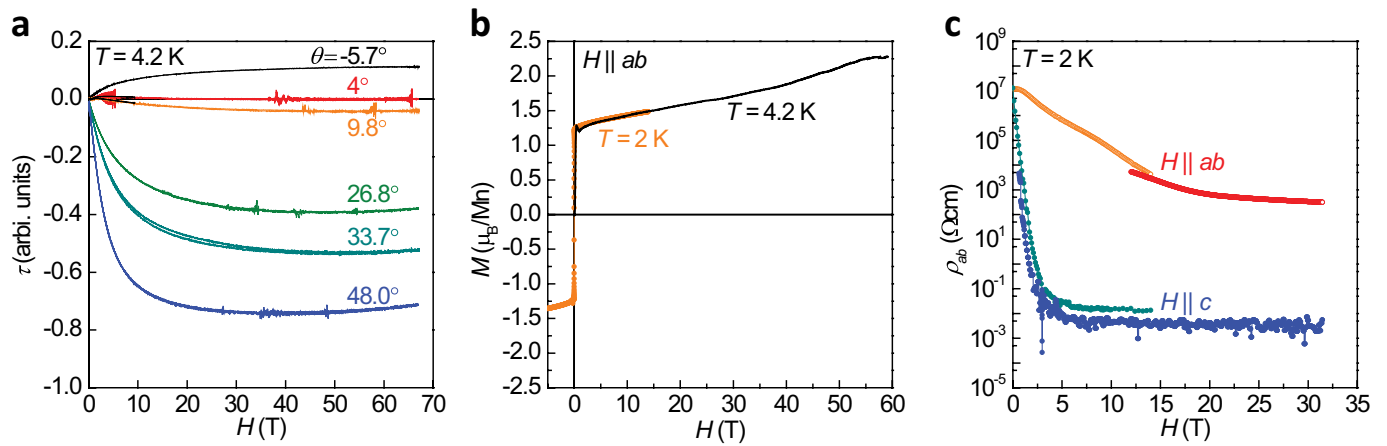
Extended Data Fig. 4 | Electronic conduction of $Mn_3Si_2Te_6$ under magnetic fields. a-f, Temperature dependent in-plane resistivity $\rho_{ab}(T)$ (left panel) and its first derivative $d\rho_{ab}(T)/dT$ (right panel) for undoped (upper), Ge-doped (middle) and Se-doped (lower) $Mn_3Si_2Te_6$ at different magnetic fields and

orientations, $H \parallel ab$ (a-c) and $H \parallel c$ (d-f). The estimated T_c is indicated by the arrows. g-i, Magnetic field dependent T_c for $H \parallel ab$ and $H \parallel c$. The errors in the experimental data are smaller than the size of the points.



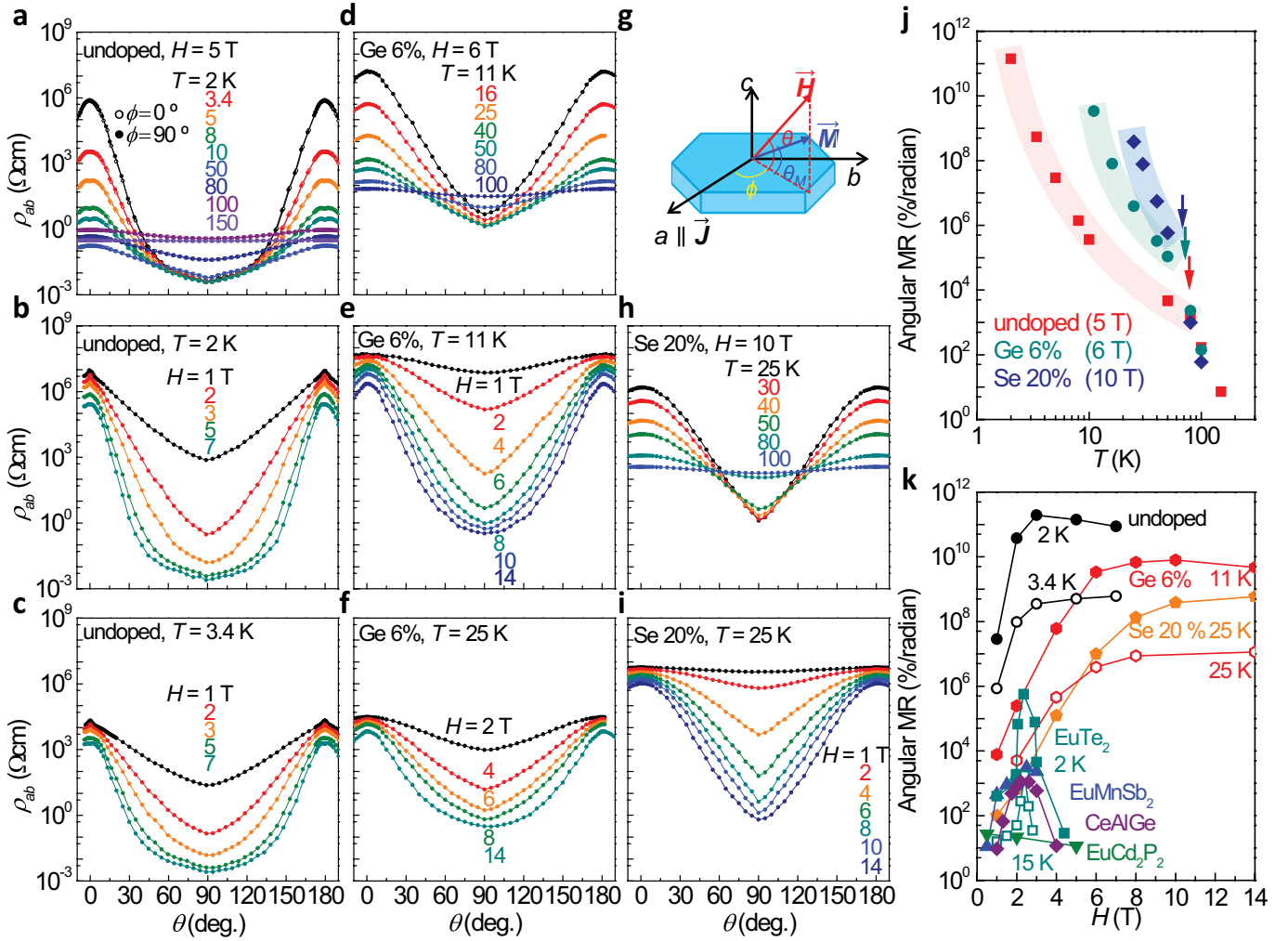
Extended Data Fig. 5 | Magnetic field dependent semiconducting conduction in $\text{Mn}_3\text{Si}_2\text{Te}_6$. **a-c**, Arrhenius plot of $\rho_{ab}(T)$ for $H \parallel ab$ (left panel) and $H \parallel c$ (right panel) at various magnetic fields for the undoped (a), Ge-doped (b) and Se-doped (c) $\text{Mn}_3\text{Si}_2\text{Te}_6$. **d-f**, Magnetic field dependent activation gap

$\Delta(H)$, extracted from the Arrhenius plot of $\rho_{ab}(T)$, for $H \parallel c$ (solid symbols) and $H \parallel ab$ (open symbols). The errors in the experimental data are smaller than the size of the points.



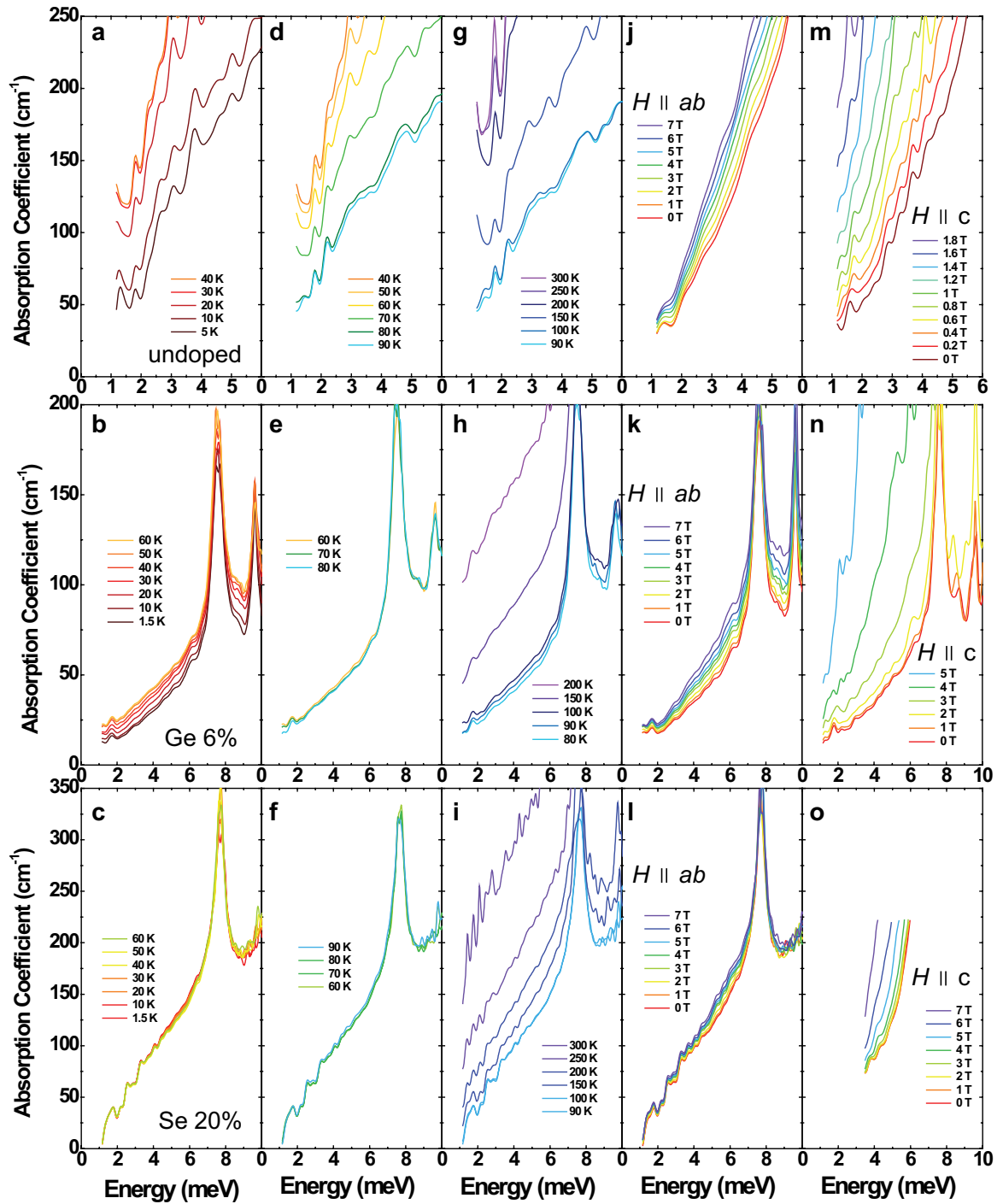
Extended Data Fig. 6 | Magnetic and magnetotransport properties of $\text{Mn}_3\text{Si}_2\text{Te}_6$ at high magnetic fields. **a**, Magnetic field dependent torque magnetometry $\tau(H)$ for different field angle θ with respect to the ab -plane. No signature of the ferrimagnetic-to-ferromagnetic transition is observed up to $H = 70$ T. **b**, Magnetic field dependent magnetization $M(H)$, taken under pulsed magnetic fields at $T = 4.2$ K (black line). Magnetization $M(H)$ under static

magnetic fields is also plotted for comparison (orange symbol). **c**, Magnetic field dependent in-plane resistivity $\rho_{ab}(H)$ for $H \parallel ab$ and $H \parallel c$. For $H \parallel ab$, the resistivity $\rho_{ab}(H)$ exhibits a relatively slow decrease with magnetic fields up to ~ 30 T, while rapid reduction of $\rho_{ab}(H)$ for $H \parallel c$ induces the insulator-to metal-transition at $H = 4$ T.



Extended Data Fig. 7 | Temperature- and magnetic field-dependent angular magnetoresistance. **a–i**, Angle dependent resistivity $\rho_{ab}(\theta)$ at various temperatures and magnetic fields for undoped (**a–c**), Ge-doped (**d–f**) and Se-doped (**h, i**) samples. The tilting angle of the external magnetic field (θ) with respect to the ab -plane and its azimuthal angle ϕ against the current direction are illustrated in **g**. For the undoped sample, $\rho_{ab}(\theta)$ taken for two different azimuthal angle $\phi = 0^\circ$ ($M \parallel J$, open symbol) and 90° ($M \perp J$, solid symbol) are

almost identical. **j**, Angular magnetoresistance (MR) $(1/\rho_{\min})d\rho(\theta)/d\theta$ as a function of temperature under $H = 5$ T (undoped), 6 T (Ge-doped) and 10 T (Se-doped). The arrows indicate T_c at zero magnetic field. **k**, Angular MR of the undoped and doped $\text{Mn}_3\text{Si}_2\text{Te}_6$ as a function of magnetic field. Angular MR of Eu-based antiferromagnets and topological magnet candidate CeAlGe are also plotted for comparison^{19,41,42,44}.



Extended Data Fig. 8 | Terahertz absorption spectroscopy. a–i, Absorption coefficient as a function of energy under zero magnetic field for undoped, Ge-doped and Se-doped $\text{Mn}_3\text{Si}_2\text{Te}_6$ taken at various temperatures. j–o, Absorption coefficient as a function of energy for the undoped (upper panel),

Ge-doped (middle panel) and Se-doped (lower panel) $\text{Mn}_3\text{Si}_2\text{Te}_6$ taken at $T = 1.5$ K for $H \parallel ab$ (j–l) and $H \parallel c$ (m–o). The peaks that appear in the case of the doped samples are infrared-active transverse optical (TO) phonon modes.

Extended Data Table 1 | Characteristic parameters of the undoped, Ge-doped and Se-doped $\text{Mn}_3\text{Si}_2\text{Te}_6$ including the ferrimagnetic transition temperature (T_c), the saturated magnetization (M_{sat}) and fields (H_{sat}) along the c-axis and the ab-plane, the magnetocrystalline anisotropy energy (K), the activation gap above T_c (Δ_{PM}) and below T_c (Δ), and the temperature scale T_0 of the ES-VRH model

Material	T_c	M_{sat}	$H_{\text{sat}}(\parallel c)$	$H_{\text{sat}}(\parallel ab)$	K	Δ_{PM}	Δ_0	T_{ES}
	(K)	(μ_{B})	(T)	(T)	(J/cm^3)	(meV)	(meV)	(K)
undoped	78	1.49	10	0.1	0.68	41	4.3	1444
Ge 6%	72	1.56	10.7	0.1	0.76	81	14.2	4384
Se 20%	68	1.44	10.4	0.1	0.68	89	26.0	8591

Article

Extended Data Table 2 | Magnetoresistance (MR) and angular MR of various magnetic materials. For each case, the magnetic phase, the magnetic ordering temperature (T_c or T_N), the MR, the angular MR, and the corresponding temperature (T) and magnetic field (H) are listed

Material	Magnetism	T_c or T_N (K)	T (K)	H (T)	MR (%)	Angular MR (% per radian)	Ref
Co ₂ MnAl					0.1	0.14	
Co ₂ Mn(Al _{0.9} Si _{0.1})	FM	693-985	300 K	2 T	0.2	0.04	[38]
Co ₂ Mn(Al _{0.5} Si _{0.5})					0.1	0.19	
Co ₂ MnSi					0.02	0.1	
La _{0.69} Ca _{0.31} MnO ₃	FM	220	225 K	1 T	1800	207	[40]
La _{0.7} Ca _{0.3} MnO _δ	FM	151	160 K	3 T	2500	38	[39]
La _{0.7} Sr _{0.3} MnO ₃	FM	-	4 K	0.3 T	0.15	0.09	[55]
				0.5 T	820	27	
EuCd ₂ P ₂	AFM	151	18 K	2 T	3900	22	[41]
				5 T	5700	12	
EuMnSb ₂	AFM	350	2 K	2.5 T	330	3000	[42]
Sr ₂ IrO ₄	AFM	240	35 K	0.25 T	300	230	[37]
				1 T	70	690	
		11	1.8 K	2 T	800	2×10^5	[43]
EuTe ₂	AFM			5 T	1.1×10^7	2.2	
		11.2	2 K	2.35 T	2.2×10^5	5.7×10^5	[44]
			15 K	2.4 T	6300	1700	
CeAlGe	Ferri	5.6	2 K	2.2 T	10	1200	[19]
				1 T	2.2×10^6	2.9×10^7	
				2 T	5.7×10^9	3.8×10^{10}	
Mn ₃ Si ₂ Te ₆	Ferri	78	2 K	3 T	9.6×10^{10}	1.9×10^{11}	This work
				5 T	3.6×10^{11}	1.4×10^{11}	
				7 T	6.1×10^{11}	8.7×10^{10}	